doi: 10.32023/0001-5237/72.3.4

ACTA ASTRONOMICA
Vol. **72** (2022) pp. 195–232

A Method of Improving Standard Stellar Luminosities with Multiband Standard Bolometric Corrections

V. Bakış and Z. Eker

Department of Space Sciences and Technologies, Faculty of Sciences,
Akdeniz University, Antalya, TR

Received April 4, 2022

ABSTRACT

Standard luminosity (L) of 406 main-sequence stars with the most accurate astrophysical parameters are calculated from their absolute magnitudes and bolometric corrections at Johnson BV, and Gaia EDR3 G, $G_{\rm BP}$, $G_{\rm RP}$ filters. Required multiband BC and $BC-T_{\rm eff}$ relations are obtained first from the parameters of 209 Double-lined Detached Eclipsing Binaries with main-sequence components and Gaia EDR3 parallaxes. A simplified SED is formulated to give filter dependent component light contributions and interstellar dimming, which are essential in computing BC of a component, virtually at any filter. The mean standard L of a star is calculated from the mean $M_{\rm bol}$ which is a mathematical average of independent $M_{\rm bol}$ values predicted at different filters, while the uncertainty of L is the uncertainty propagated from the uncertainty of the mean $M_{\rm bol}$. The mean standard L of the sample stars are compared to the corresponding L values according to the Stefan-Boltzmann law. A very high correlation ($R^2 > 0.999$) is found. Comparing histogram distributions of errors shows that uncertainties associated with the mean standard L (peak at ≈ 2.5 per cent) are much smaller than the uncertainties of L (peak at ≈ 8 per cent) by the Stefan-Boltzmann law. Increasing the number of filters used in predicting the mean $M_{\rm bol}$ increases the accuracy of the standard stellar luminosity. Extinction law, color–color relations and color excess *vs.* color excess relations for Gaia passbands are presented for the first time for main-sequence stars.

Key words: *Stars: fundamental parameters – binaries: eclipsing – Sun: general*

1. Introduction

An unobserved missing fraction of a stellar luminosity (L) by a photometric observation is named bolometric correction (BC) if it is expressed in magnitude units. As if fixing a defect or restoring the missing part, adding this fraction (BC) to the apparent (V) or absolute (M_V) magnitudes of a star, which are known to be naturally limited in a certain wavelength range, one obtains the apparent ($m_{\rm bol}$) or absolute ($M_{\rm bol}$) bolometric magnitudes representing the total L of the star. Although BC

is useful, ingeniously invented, and the ready-to-use quantity to obtain those quantities from an apparent magnitude (V) and a parallax, major difficulty confronted by the earlier astronomers (Kuiper 1938, Mc Donald and Underhill 1952, Popper 1959, Wildey 1963, Smak 1966, Johnson 1966, Weidemann and Bues 1967, Heintze 1973) is that a pre-required BC must be determined first from observations but there is neither a telescope nor a detector to measure a bolometric magnitude while L is already known to be un-observable.

Therefore, a relation between an apparent magnitude (*e.g.*, V) and observable part of the luminosity (*e.g.*, L_V) recognized in all of the photometric passbands with pre-established filter transmissions operated in the Vega system of magnitudes, where Vega is a common reference, cannot be established between a bolometric magnitude and L using direct observations.

This difficulty, however, was overcome by assuming arbitrary zero points for both the bolometric magnitudes and BC scale. The arbitrariness attributed to BC and bolometric magnitude scales caused then publications of many different BC tables, some containing all negative (Kuiper 1938, Popper 1959, Wildey 1963, Cox 2000, Pecaut and Mamajek 2013) BC values while others contained a limited number of positive BCs (Code *et al.* 1976, Johnson 1964, 1966, Flower 1977, 1996, Bessel *et al.* 1998, Sung *et al.* 2013, Cassagrande and VandenBerg 2018, Eker *et al.* 2020). Incorrect usage of tabulated BC values was discussed by Torres (2010). The biggest of the problems, however, is that a star could be found to have several BCs from several tables, implying that several different $M_{\rm bol}$ representing a single L.

The problems of arbitrariness attributed to the BC scale were studied recently by Eker *et al.* (2021a), who introduced the concept of standard BC. The standardization was necessary to avoid problems caused by arbitrariness of the BC scale and for unifying the BC and $M_{\rm bol}$ values, which is the easiest way of assuring consistent L of a star if it is predicted from astrometric (parallax) and photometric observations.

Accuracy of the classical methods of computing a stellar luminosity (1 – a direct method from radii (R) and effective temperatures ($T_{\rm eff}$), 2 – a method using a mass–luminosity relation (MLR), 3 – a method requiring a bolometric correction) was later studied by Eker *et al.* (2021b), who introduced the concept of standard stellar L. If L of a star is calculated from one of its absolute magnitudes (M_ξ, where ξ indicates a filter in a photometric system) and corresponding standard BC, it is called standard L while L according to the Stefan-Boltzmann law is standard by definition.

The methods (2) and (3) are indirect because a pre-determined MLR is required for method (2) and a pre-determined $BC - T_{\rm eff}$ relation is necessary for method (3). In the absence of these pre-determined relations, both are not operable.

Eker *et al.* (2021b) claimed the indirect methods are less accurate than the direct method providing a stellar L with a typical accuracy of 8.2–12.2 per cent, which

could be as high as a few per cent, *e.g.*, primary of V505 Per has $L = 2.688\ \mathrm{L}_{\odot}$ and its uncertainty ($\Delta L/L$) is 2.53 per cent implied by very small relative uncertainties of its radius $\Delta R/R = 1.09$ per cent and effective temperature $\Delta T_{\rm eff}/T_{\rm eff} = 0.32$ per cent (Tomasella *et al.* 2008). Only if a unique *BC* directly determined from an observed SED with very high spectral resolution is used in the third method, then the relative uncertainty of predicted L could be improved up to a level of about one per cent. Otherwise, using a standard *BC* predicted from the standard $BC - T_{\rm eff}$ relation, method (3) cannot provide an accuracy better than the direct method.

However, using a unique *BC* in method (3) is just a speculation, that is, it is impractical nowadays as expressed by Eker *et al.* (2021b). Therefore, the primary aim of this study is not to speculate, but to investigate how to improve the standard stellar luminosities obtained by the third method using realistic multiband standard $BC-T_{\rm eff}$ relations. To achieve this aim, a new method is introduced for estimating relative light contributions of binary components from a simplified SED, operable virtually at any photometric passband. Then, the classical method of Eker *et al.* (2020), which requires an apparent magnitude of a binary system, the light ratio of components, a reliable parallax and an interstellar extinction, is used for predicting the multiband $BC-T_{\rm eff}$ relations for the Gaia G, $G_{\rm BP}$ and $G_{\rm RP}$, and Johnson *B*, *V* passbands. Data and input parameters are described in Section 2. The new method is explained in Section 3. Calibrations of multiband $BC-T_{\rm eff}$ relations are described in Section 4. How to improve standard L of a star is discussed in Section 5. Discussions are found in Section 6. Conclusions are in Section 7.

2. Data

Having essentially the same purpose, to obtain the most reliable empirical *BC* from the most reliable stellar parameters and then to calibrate the most reliable $BC-T_{\rm eff}$ relations, this study and Eker *et al.* (2020) rely upon the same original data set of Double-Lined Detached Eclipsing Binaries (DDEB) published by Eker *et al.* (2018). 509 main-sequence stars in the solar neighborhood of the Galactic disk – the components of DDEBs – with most reliable masses (M) and radii (R) accurate within 15 per cent and with published effective temperatures ($T_{\rm eff}$) having metallicities $0.008 \leq Z \leq 0.040$ were originally used by Eker *et al.* (2018) for calibrating interrelated mass–luminosity (MLR), mass–radius (MRR) and mass *vs.* effective temperature (MTR) relations. Later, Eker *et al.* (2020) combined this data set with the data set of Graczyk *et al.* (2019), who studied the global zero-point shift between the photometric fluxes of 81 detached eclipsing binaries and Gaia DR2 trigonometric parallaxes (Gaia Collaboration *et al.* 2018) in order to increase the number of available systems with component light ratios in Johnson *B*- and *V*-bands, essential for computing the apparent magnitude of a component from the total brightness of a system – a step required before computing *BC* of a component.

This combined data set of Eker *et al.* (2020) contained 290 DDEB having at least one component on the main sequence. Aiming to calibrate a main-sequence $BC_V - T_{\rm eff}$ relation, Eker *et al.* (2020) could find only 400 main-sequence stars (194 binaries, 8 primaries, and 4 secondaries, that is, 206 systems) from the available 580 component stars (290 DDEB). 290 minus 206, that is, 84 systems were lost because of a missing systemic apparent brightness (V_{tot}), or a missing light ratio (l_2/l_1) in the *V*-band, or a missing parallax, or a missing interstellar dimming (A_V). If any one of those parameters is missing for a system, *BC* of its components cannot be calculated, that is, this system is not eligible for calculating *BC*. A percentage of a third light is also needed if it is detected in the light curve of a system. 206 DDEB has 412 components. After subtracting the non-main-sequence stars, the number of stars with a computed BC_V reduced to 400, from which a main-sequence $BC_V - T_{\rm eff}$ relation is calibrated by Eker *et al.* (2020).

The original data set containing 290 systems investigated by Eker *et al.* (2020) is considered for this study for two purposes: First of all, we wanted to test whether or not the new method used in this study provides reliable component light contributions. For this, 206 systems with *V* and *B*-passband light ratios published by Eker *et al.* (2020) are ideal for testing by comparing to the light ratios found in this study. Nevertheless, the new method also has its own limitations, to be discussed in the next section. That is, 206 systems will naturally be reduced further. To compensate for such a further loss and to be able to use its applicability to the systems even without standard *V* light curve solutions, the larger data set (290 system) was chosen as the main sample for this study.

Here in this study, nearly the same number (406) of main-sequence stars are found as the components of 209 DDEB (197 system, 9 primaries and 3 secondaries) eligible to calculate their *BC* values and then to continue calibrating $BC - T_{\rm eff}$ relations for the Gaia photometric passbands G, $G_{\rm BP}$ and $G_{\rm RP}$. Among this subsample 312 main-sequence stars (152 binaries, 5 primaries and 3 secondaries) are found as a sub sub-sample containing stars common between the present study and Eker *et al.* (2020), which are sufficient for testing and verifying the validity of the component contributions predicted by the new method involving SED.

The basic physical parameters of the components and total brightness in *B*, *V* and Gaia passbands of DDEBs used in this study are listed in Table 1. Order, name of the system, the component (primary or secondary) are listed in the first three columns. Note that the primaries and the secondaries identified as non-main-sequence stars are indicated by p* or s*. From the fourth to seventh columns, masses and radii with their errors are given. In columns 9 and 10, temperatures and errors are given. References for physical parameters are listed in columns 8 and 11. The total brightness of the systems in *B*- and *V*-bands with their errors are provided in columns 12–15 with their references in the 16th column. In the rest of the columns (17–22), the total brightness of the systems in the Gaia passbands which are available in the Gaia EDR3 are given.

Table 1

Physical parameters and total magnitudes of selected systems in B, V, G, $G_{\rm BP}$ and $G_{\rm RP}$

Order	Name	pri/sec	M [$M_\odot$]	err [$M_\odot$]	R [$R_\odot$]	err [$R_\odot$]	Reference	T [K]	err [K]	Reference	B [mag]	err [mag]	V [mag]	err [mag]	Reference	G [mag]	err [mag]	$G_{\rm BP}$ [mag]	err [mag]	$G_{\rm RP}$ [mag]	err [mag]
1	V421 Peg	p	1.594	0.029	1.584	0.028	2016NewA...46...47O	7250	80	2016NewA...46...47O	8.650	0.010	8.280	0.010	2016NewA...46...47O	8.208	0.003	8.384	0.003	7.890	0.004
2	V421 Peg	s	1.356	0.029	1.328	0.029	2016NewA...46...47O	6980	120	2016NewA...46...47O	8.650	0.010	8.280	0.010		8.208	0.003	8.384	0.003	7.890	0.004
3	DV Psc	p	0.677	0.019	0.685	0.030	2014PASA...31...24E	4450	8	2007MNRAS.382.1133Z	11.604	0.010	10.621	0.010	2000A&A...355L..27H	10.219	0.005	10.997	0.015	9.334	0.013
4	DV Psc	s	0.475	0.010	0.514	0.020	2014PASA...31...24E	3614	8	2007MNRAS.382.1133Z	11.604	0.010	10.621	0.010		10.219	0.005	10.997	0.015	9.334	0.013
5	MU Cas	p	4.657	0.100	4.192	0.050	2014PASA...31...24E	14750	500	2004AJ....128.1840L	11.112	0.009	10.808	0.007	2019ApJ...872...85G	10.742	0.003	10.894	0.003	10.452	0.004
...	...	...	...	...	...	...	...	...	...	...	...	...	...	...	...	...	...	...	...	...	...
414	AP And	s	1.251	0.004	1.195	0.005	2014AJ....147..148L	6495	150	2014AJ....147..148L	11.606	0.057	11.074	0.085		10.910	0.003	11.195	0.003	10.457	0.004
415	AL Scl	p	3.617	0.110	3.241	0.050	2014PASA...31...24E	13550	350	1987A&A...179..141H	5.985	0.014	6.070	0.009	2000A&A...355L..27H	6.073	0.003	6.017	0.004	6.145	0.004
416	AL Scl	s	1.703	0.040	1.401	0.020	2014PASA...31...24E	10300	360	1987A&A...179..141H	5.985	0.014	6.070	0.009		6.073	0.003	6.017	0.004	6.145	0.004
417	V821 Cas	p	2.025	0.066	2.308	0.028	2014PASA...31...24E	9400	400	2009MNRAS.395.1649C	8.402	0.029	8.286	0.017	2019ApJ...872...85G	8.227	0.003	8.265	0.003	8.121	0.004
418	V821 Cas	s	1.620	0.058	1.390	0.022	2014PASA...31...24E	8600	400	2009MNRAS.395.1649C	8.402	0.029	8.286	0.017		8.227	0.003	8.265	0.003	8.121	0.004

Table 2

Component apparent magnitudes of DDEB in B, V, G, $G_{\rm BP}$ and $G_{\rm RP}$ according to component contributions estimated by the new method using simplified SED

Order	Name	pri/sec	Cross Reference		Cont. (Eker *et al.* 2020)		Unreddened light contribution (this study)					Component apparent brightness [mag]									
			Xref 1	Xref 2	l_B	l_V	l_B	l_V	l_G	$l_{G_{\rm BP}}$	$l_{G_{\rm RP}}$	B	err	V	err	G	err	$G_{\rm BP}$	err	$G_{\rm RP}$	err
1	V421 Peg	p	1	1	–	0.624	0.630	0.622	0.621	0.625	0.614	9.152	0.010	8.796	0.010	8.725	0.003	8.894	0.003	8.421	0.004
2	V421 Peg	s	2	1	–	0.376	0.370	0.378	0.379	0.375	0.386	9.729	0.010	9.335	0.010	9.261	0.003	9.449	0.003	8.923	0.004
3	DV Psc	p	5	2	0.918	0.889	0.906	0.873	0.852	0.878	0.826	11.711	0.010	10.768	0.010	10.393	0.005	11.138	0.015	9.541	0.013
4	DV Psc	s	6	2	0.082	0.111	0.094	0.127	0.148	0.122	0.174	14.166	0.010	12.861	0.010	12.294	0.005	13.284	0.015	11.233	0.013
5	MU Cas	p	7	3	0.556	0.557	0.551	0.554	0.553	0.552	0.556	11.758	0.009	11.450	0.007	11.385	0.003	11.539	0.003	11.090	0.004
...	...	...	...	...	...	...	...	...	...	...	...	...	...	...	...	...	...	...	...	...	...
414	AP And	s	582	204	0.470	0.471	0.471	0.473	0.474	0.472	0.476	12.424	0.057	11.886	0.085	11.721	0.003	12.010	0.003	11.263	0.004
415	AL Scl	p	583	205	0.960	0.950	0.924	0.914	0.916	0.920	0.904	6.070	0.014	6.167	0.009	6.169	0.003	6.107	0.004	6.255	0.004
416	AL Scl	s	584	205	0.040	0.050	0.076	0.086	0.084	0.080	0.096	8.790	0.014	8.738	0.009	8.760	0.003	8.764	0.004	8.685	0.004
417	V821 Cas	p	585	206	0.797	0.779	0.794	0.784	0.785	0.789	0.774	8.652	0.029	8.550	0.017	8.490	0.003	8.522	0.003	8.400	0.004
418	V821 Cas	s	586	206	0.203	0.221	0.206	0.216	0.215	0.211	0.226	10.120	0.029	9.951	0.017	9.893	0.003	9.957	0.003	9.736	0.004

Full versions of Tables 1 and 2 are available form the *Acta Astronomica Archive* (see cover page)

Table 3

Component absolute magnitudes of DDEB in B, V, G, $G_{\rm BP}$ and $G_{\rm RP}$ and propagated uncertainties

Order	Name	pri/sec	Parallax [mas]	$\frac{\sigma_{\varpi}}{\varpi}$ [%]	$L/L_{\odot}$	L(SI) $\times 10^{27}$	$\frac{\Delta L}{L}$ [%]	$M_{\rm bol}$ [mag]	err [mag]	A_B [mag]	A_V [mag]	A_G [mag]	$A_{G_{\rm BP}}$ [mag]	$A_{G_{\rm RP}}$ [mag]	M_B [mag]	err [mag]	M_V [mag]	err [mag]	M_G [mag]	err [mag]	$M_{G_{\rm BP}}$ [mag]	err [mag]	$M_{G_{\rm RP}}$ [mag]	err [mag]
1	V421 Peg	p	6.5051	0.4	6.245	2.390	6	2.751	0.061	0.122	0.092	0.087	0.104	0.057	3.096	0.042	2.770	0.042	2.704	0.041	2.857	0.041	2.430	0.041
2	V421 Peg	s	6.5051	0.4	3.771	1.444	8	3.299	0.088	0.122	0.092	0.087	0.104	0.057	3.673	0.042	3.310	0.042	3.240	0.041	3.412	0.041	2.932	0.041
3	DV Psc	p	23.7216	0.1	0.166	0.063	9	6.691	0.095	0.800	0.603	0.492	0.633	0.368	7.787	0.041	7.041	0.041	6.777	0.040	7.381	0.043	6.049	0.042
4	DV Psc	s	23.7216	0.1	0.041	0.016	8	8.219	0.085	0.800	0.603	0.492	0.633	0.368	10.242	0.041	9.134	0.041	8.678	0.040	9.528	0.043	7.741	0.042
5	MU Cas	p	0.5133	3.7	749.386	286.827	14	−2.447	0.149	1.644	1.233	1.243	1.446	0.776	−1.333	0.091	−1.231	0.090	−1.305	0.090	−1.356	0.090	−1.133	0.090
...	...	...	...	...	...	...	...	...	...	...	...	...	...	...	...	...	...	...	...	...	...	...	...	...
414	AP And	s	2.9143	0.7	2.291	0.877	9	3.840	0.101	0.406	0.306	0.282	0.341	0.190	4.340	0.071	3.903	0.095	3.762	0.043	3.991	0.043	3.395	0.043
415	AL Scl	p	4.6006	3.6	319.014	122.103	11	−1.519	0.117	0.041	0.031	0.032	0.037	0.020	−0.657	0.090	−0.550	0.089	−0.549	0.088	−0.616	0.089	−0.451	0.089
416	AL Scl	s	4.6006	3.6	19.903	7.618	14	1.493	0.155	0.041	0.031	0.032	0.037	0.020	2.063	0.090	2.021	0.089	2.042	0.088	2.042	0.089	1.979	0.089
417	V821 Cas	p	3.4262	0.6	37.469	14.341	17	0.806	0.187	0.123	0.092	0.092	0.107	0.058	1.203	0.051	1.132	0.045	1.072	0.042	1.089	0.042	1.016	0.042
418	V821 Cas	s	3.4262	0.6	9.522	3.644	19	2.293	0.205	0.123	0.092	0.092	0.107	0.058	2.671	0.051	2.532	0.045	2.475	0.042	2.524	0.042	2.352	0.042

Eleven DR2 and one Hipparcos parallaxes are shown in square brackets and parenthesis, respectively.

Table 4

Empirical standard component BCs of DDEB in B, V, G, $G_{\rm BP}$ and $G_{\rm RP}$ and propagated uncertainties

Order	Name	pri/sec	BC_B [mag]	err [mag]	BC_V [mag]	err [mag]	BC_G [mag]	err [mag]	$BC_{G_{\rm BP}}$ [mag]	err [mag]	$BC_{G_{\rm RP}}$ [mag]	err [mag]	$(B-V)_0$ [mag]	$(V-G)_0$ [mag]	$(G-G_{\rm BP})_0$ [mag]	$(G-G_{\rm RP})_0$ [mag]	$(G_{\rm BP}-G_{\rm RP})_0$ [mag]
1	V421 Peg	p	−0.345	0.074	−0.019	0.070	0.047	0.069	−0.105	0.074	0.322	0.065	0.326	0.066	−0.152	0.275	0.427
2	V421 Peg	s	−0.374	0.098	−0.011	0.094	0.059	0.094	−0.113	0.097	0.367	0.091	0.363	0.070	−0.172	0.308	0.480
3	DV Psc	p	−1.096	0.104	−0.350	0.101	−0.085	0.100	−0.689	0.105	0.642	0.098	0.746	0.265	−0.604	0.728	1.332
4	DV Psc	s	−2.023	0.095	−0.916	0.091	−0.460	0.090	−1.309	0.095	0.478	0.088	1.108	0.456	−0.849	0.938	1.787
5	MU Cas	p	−1.113	0.175	−1.216	0.173	−1.141	0.173	−1.091	0.175	−1.313	0.171	−0.102	0.075	0.050	−0.172	−0.222
...	...	...	...	...	...	...	...	...	...	...	...	...	...	...	...	...	...
414	AP And	s	−0.500	0.123	−0.063	0.136	0.078	0.106	−0.151	0.110	0.445	0.104	0.437	0.141	−0.229	0.367	0.597
415	AL Scl	p	−0.863	0.147	−0.970	0.145	−0.970	0.144	−0.903	0.147	−1.069	0.143	−0.107	0.000	0.067	−0.099	−0.165
416	AL Scl	s	−0.570	0.179	−0.528	0.177	−0.549	0.176	−0.549	0.178	−0.486	0.175	0.042	-0.021	0.000	0.063	0.063
417	V821 Cas	p	−0.397	0.194	−0.326	0.190	−0.267	0.190	−0.283	0.191	−0.210	0.188	0.071	0.059	−0.016	0.057	0.073
418	V821 Cas	s	−0.377	0.211	−0.239	0.208	−0.182	0.208	−0.230	0.209	−0.059	0.206	0.138	0.057	−0.048	0.123	0.172

Full versions of Tables 3 and 4 are available form the *Acta Astronomica Archive* (see cover page)

In Table 2, in addition to the first three columns which are the same as in Table 1, the fourth and fifth columns give cross references where Xref(1) (column 4) indicates the order number in Eker *et al.* (2018) and Xref(2) (column 5) indicates the order number in Eker *et al.* (2020). Every system in this study has at least one Xref number in columns 4 and 5. Only five binaries from the list of Graczyk *et al.* (2019) do not have Xref in column 4. Systems without Xref numbers in column 5 are the ones excluded by Eker *et al.* (2020) either because of missing *V*-band light ratio or without interstellar extinction etc. In this study, we preferred to display component contributions (columns 6 and 7) rather than light ratios which were preferred by Eker *et al.* (2020). Thus, the sum of the contributions of the primary and the secondary is one.

The advantage here is that the component contributions of all systems in Table 2 are predictable by the new method. There are two possibilities for this: from the reddened SED, and the other from the unreddened SED. The unreddened light contributions are listed in Table 2 (columns 8, 9, 10, 11, 12) for *B*, *V*, *G*, $G_{\rm BP}$ and $G_{\rm RP}$ passbands, respectively. Since reddened component contributions are the same in four digits after the decimal, to save space, they are not shown in Table 2.

At last, component apparent magnitudes in accord with the contributions are given in columns 13, 15, 17, 19 and 21 for the same bands in the same order. Rather than propagating observational random errors, Eker *et al.* (2020) had no option but to assume the same uncertainty for the component magnitudes as the systemic brightness because the light ratio (L_2/L_1) of components predicted from

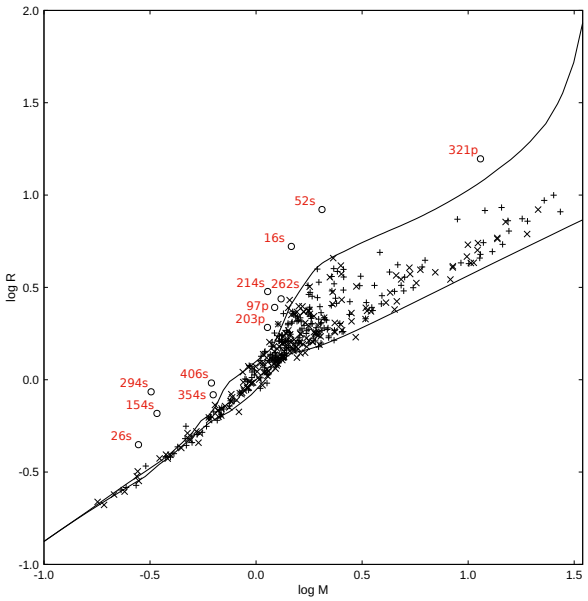

Fig. 1. Primary (+) and secondary (x) components on the main-sequence and components discarded (empty circles). Numbers are in the order in Table 1, p and s for primary and secondary. Solid lines show ZAMS and TAMS limits for solar metallicity ($Z = 0.014$).

light curve solutions are usually published without an uncertainty. Using the same method here, the same steps are followed in this study. That is, the uncertainty of the component magnitudes were assumed to have the same uncertainty as the uncertainty of the systemic brightness.

One may notice that many systems in Table 2 do not have *B*-band apparent magnitudes (column 13) in contrast to apparent magnitudes at Gaia passbands, which are almost complete excluding only β Aur and α CrB (both are too bright for reliable measurement), while ten systems have missing *V*-band magnitude.

There are eleven more systems, including VV Pyx, (marked in Table 3) which do not produce reliable SED model with EDR3 parallaxes. DR2 parallaxes produce better SED model in this cases. For VV Pyx, β Aur and α CrB we found better SED models with Hipparcos parallaxes.

Before going to the next section, where the new method is described, we must certify the 406 stars considered in this study are all in the main-sequence stage of evolution, which is very obvious in Fig. 1. The three primaries and nine secondaries identified as non-main-sequence stars appear located outside of the main-sequence limits, which are shown by continuous lines, according to ZAMS (Zero Age Main Sequence) and TAMS (Terminal Age Main Sequence) limits for the solar abundance $Z = 0.014$ from PARSEC evolutionary models (Bressan *et al.* 2012).

Metal abundance distribution of DDEB at the solar neighborhood within the disk of the Milky Way has already been discussed by Eker *et al.* (2018), where the peak at the solar metallicity ($Z = 0.014-0.017$) together with the lower ($Z = 0.008$) and the upper ($Z = 0.040$) limits were indicated. To save space and to be clearer at identifications of non-main-sequence stars in Fig. 1, the ZAMS and TAMS curves for $Z = 0.008$, $Z = 0.040$ and discussions therein are not repeated in this study. However, because the present sub-sample is mainly selected from the sample of Eker *et al.* (2018), metal abundances of the main-sequences stars used in this study are also expected to have a similar metallicity distribution within the limits $0.008 \leq Z \leq 0.040$.

3. A New Method Involving SED to Obtain Light Ratio of Components

When computing *BC* of stars, unlike previous studies (Code *et al.* 1976, Cayrel *et al.* 1997, Girardi *et al.* 2008, Andrae *et al.* 2018, Chen *et al.* 2019) utilizing the well-known relation directly with $S_\lambda(V)$ (sensitivity function of the *V* magnitude system), f_λ, (monochromatic flux from a star), $f_{\rm bol}$, (bolometric flux of a star reaching the telescope if there is no extinction), and C_2 (arbitrary constant of integration),

$$BC_V = 2.5 \log \frac{f_V}{f_{\rm bol}} + C_2 = 2.5 \log \frac{\int_0^\infty S_\lambda(V) f_\lambda \, {\rm d}\lambda}{\int_0^\infty f_\lambda \, {\rm d}\lambda} + C_2, \qquad (1)$$

here, we introduce a new method operating indirectly. This new method deserves to be called indirect because the V filtered radiation

$$f_V = \int_0^\infty S_\lambda(V)\, f_\lambda \, \mathrm{d}\lambda, \tag{2}$$

is calculated using the SED model with simplifications only for predicting relative light contributions (to be explained later) of component stars in binaries. Only after, apparent magnitudes of the components calculated from apparent magnitude of the system using the light ratio of components, and absolute magnitudes are calculated from the apparent magnitudes as being corrected for interstellar extinction, BC of each component is calculated as

$$BC_V = M_{\mathrm{bol}} - M_V. \tag{3}$$

The first simplification is that the spectrum of a component (f_λ) is approximated by a Planck Function, rather than a model atmosphere characterized by a T_{eff}, $\log g$, micro-turbulent velocity (ζ) and metal abundance [Fe/H]. Being independent of model atmosphere parameters, the new method is easier to use and more suitable for obtaining empirical BCs, *e.g.*, for main-sequence stars, rather than series of BC tables specified with a $\log g$, ζ or [Fe/H] for various passbands of different photometric systems.

Assuming no interstellar extinction in the first approximation, a spherical star with a radius R produces a flux continuum (SED) at a distance d from its center. The monochromatic flux could be expressed as:

$$f_\lambda = \frac{R^2}{d^2} \pi B_\lambda(T_{\mathrm{eff}}). \tag{4}$$

Then, the second simplification becomes clear, the spectral lines and prominent spectral features are ignored since the Plank function represents the star's continuum. The equation implies that limb darkening is also ignored within the solid angle $\pi R^2/d^2$ where the isotropic intensity is $B_\lambda(T_{\mathrm{eff}})$. Eq.(4) would be adapted to a detached binary with spherical components as:

$$f_\lambda(\mathrm{system}) = \frac{\pi}{d^2} \left[R_1^2 B_\lambda(T_1) + R_2^2 B_\lambda(T_2) \right], \tag{5}$$

where R_1 and R_2 and T_1 and T_2 are radii and effective temperatures of the primary and secondary, respectively. If d is also the distance from the Earth, then f_λ in both equations would represent an unreddened SED in units of W $m^{-2}A^{-1}$. The unreddened SED of V618 Per, which is one of the systems in Table 1, is shown by a dashed curve starting from the upper left and ending at the lower right in Fig. 2. The observed spectrophotometric flux data of V618 Per are taken from the SIMBAD database (Wenger *et al.* 2000). The observed flux data does not appear to fit the unreddened SED, especially toward shorter wavelengths. The deviation from the unreddened SED is expected because of interstellar extinction.

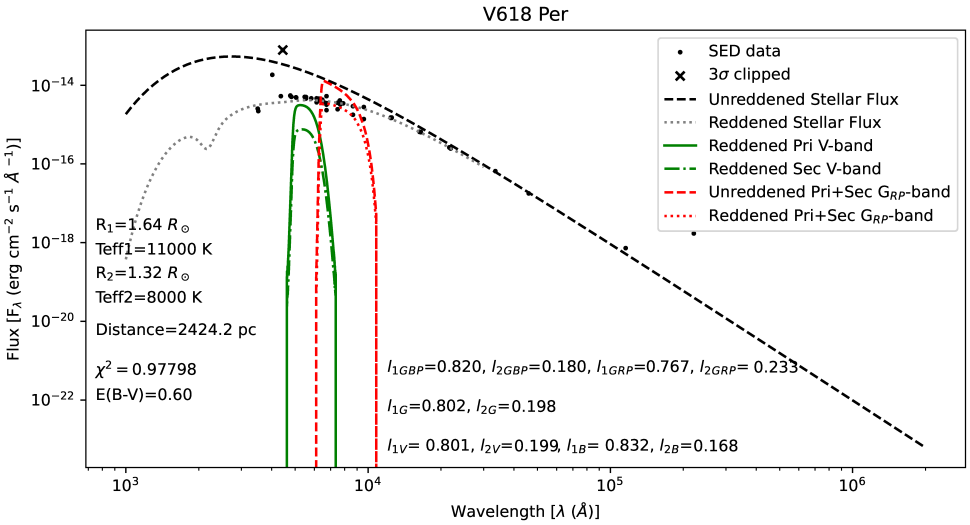

Fig. 2. Unreddened (dashed) and reddened (dotted) SED models for V618 Per. Flux data determining the reddened SED are shown by filled circles. Crosses are data deviated more than 3σ. For simplicity, only the relative *V*-band contributions of primary (continuous) and secondary (dot-dashed) are shown by vertical profiles on the left. The *G*-band dimming ($A_{G_{\rm RP}}$) is computed from the vertical profiles on the right which are the total (primary + secondary) light of the system from the reddened (dotted) and unreddened (dashed) SED after convolution by the G filter.

For modeling the observed SED data, our unreddened SED model is reddened by adjusting $E(B-V)$ of the system until a best fitting reddened SED is obtained using the reddening model of Fitzpatrick (1999). The parameter $R(V)$ is adopted as $R(V) = 3.1$. Since we have calculated the parameter $R(\lambda) = A_\lambda / E(B-V)$ for each filter individually, the initially selected value of $R(V)$ did not affect our analysis. We will discuss this issue later. The χ^2 fitting of the reddened SED is displayed by a dotted continuous curve just below the unreddened SED in Fig. 2.

Assuming no interstellar extinction, that is the previously computed unreddened SED (Eq. 5), one may compute unreddened visual flux f_V of a component, if a reliable trigonometric parallax (or distance) is available, using f_λ from Eq.(4) to indicate the flux contribution of the component in the *V* filtered radiation (SED) reaching above the Earth's atmosphere. However, by replacing the unreddened f_λ with the reddened f_λ, which is obtained by χ^2 fitting, one may compute the *V*-band flux contribution of the very same component in the reddened SED.

We have systematically calculated both reddened and unreddened component contributions at *B*, *V*, *G*, $G_{\rm BP}$ and $G_{\rm RP}$ passbands using the filter profiles from Bessel (1990) and Evans *et al.* (2018) for Johnson *B*, *V*, and Gaia passbands, respectively. For the sake of clarity, only *V*-band contributions of the primary and the secondary of V618 Per corresponding to the reddened SED are shown in Fig. 2 as vertical profiles on the left where the solid and dotted-dash lines are for primary's and secondary's contribution, respectively. Unreddened contributions of primary

and secondary are not shown for clarity. Notice that having a bigger radius and a hotter effective temperature, the primary's contribution is larger than the secondary's contribution. Relative contributions of components are given in Table 2 (columns 6–12). The relative contribution of a primary is computed as:

$$\text{Primary}'\text{s cont.} = \frac{f_\xi(\text{pri})}{f_\xi(\text{pri}) + f_\xi(\text{sec})}, \tag{6}$$

where ξ represents one of the passbands *B*, *V*, G, $G_{\rm BP}$ and $G_{\rm RP}$. Then, the secondary's relative contribution is just one minus the primary's contribution.

3.1. Multiband Standard BC_ξ by the New Method

The new method provides not only component contributions but also provides the amount of dimming due to interstellar extinction in magnitude scale (A_ξ) which is needed when computing absolute magnitude (M_ξ) of a component from its apparent magnitude ξ,

$$M_\xi = \xi + 5\log\varpi + 5 - A_\xi, \tag{7}$$

where ϖ and A_ξ are trigonometric parallax in arcseconds and interstellar extinction in magnitudes for the passband ξ, respectively. It would be clear according to Fig. 2 that

$$A_\xi = 2.5\log\frac{\int_0^\infty S_\lambda(\xi)\, f_\lambda^0(\text{system})\,\mathrm{d}\lambda}{\int_0^\infty S_\lambda(\xi)\, f_\lambda(\text{system})\,\mathrm{d}\lambda}, \tag{8}$$

where f_λ^0(system) is the unreddened SED of the system. The profile after convolution of f_λ^0(system) by the G filter is shown as the dashed vertical profile on the right in Fig. 2. f_λ (system) is the reddened SED of the system. The profile after convolution of f_λ (system) by the G filter is shown as the dotted vertical profile in Fig. 2.

The dimming (A_ξ) in each of the photometric bands *B*, *V*, G, $G_{\rm BP}$, and $G_{\rm RP}$ are calculated according to Eq.(8) and they are listed in Table 3 together with the other parameters needed for computing absolute magnitudes of the components. The first three columns are the same as in Table 2 (order, name, and p or s). Parallax and relative error of parallax are in columns 4–5. L of the components according to Stefan-Boltzmann law in Solar and SI units and its associated relative error propagated from the uncertainties of radius and $T_{\rm eff}$ are in columns 6–8. After bolometric absolute magnitudes (column 9), which are computed directly from L, using the relation suggested by IAU General Assembly Resolution B2, hereafter (IAU 2015 GAR B2)

$$M_{\rm bol} = -2.5\log L + C_{\rm bol}, \tag{9}$$

where $C_{\rm bol} = 71.197425...$ if L uses SI units, $C_{\rm bol} = 88.697425\ldots$, and if L uses cgs units (IAU 2015 GAR B2, Eker *et al.* 2021a), the interstellar extinctions (dimming) in *V*, *B*, G, $G_{\rm BP}$, and $G_{\rm RP}$ passbands are given in columns 11–15. The rest of the columns of Table 3 is reserved for the absolute magnitudes of components

in V, B, G, $G_{\rm BP}$, and $G_{\rm RP}$ bands and their associated errors. Finally, the multiband standard BC values of the component stars according to the basic definition $BC_\xi = M_{\rm bol} - M_\xi$ (multiband form of Eq. 3) are listed in Table 4, where the columns are self-explanatory, order, name, p or s, BC_B and its error, BC_V and its error, BC_G and its error, $BC_{G_{\rm BP}}$ and its error, $BC_{G_{\rm RP}}$ and its error.

3.2. Testing the New Method

Even if a zero-point error is absent, besides the propagated errors originating from the random observational uncertainties, consequence errors would also be appended to a computed BC if it is calculated directly from Eq.(1) with a simplified SED. The consequence errors are defined here to indicate errors in a computed BC if it is predicted according to Eq.(1) where the SED of the component is not its ob-

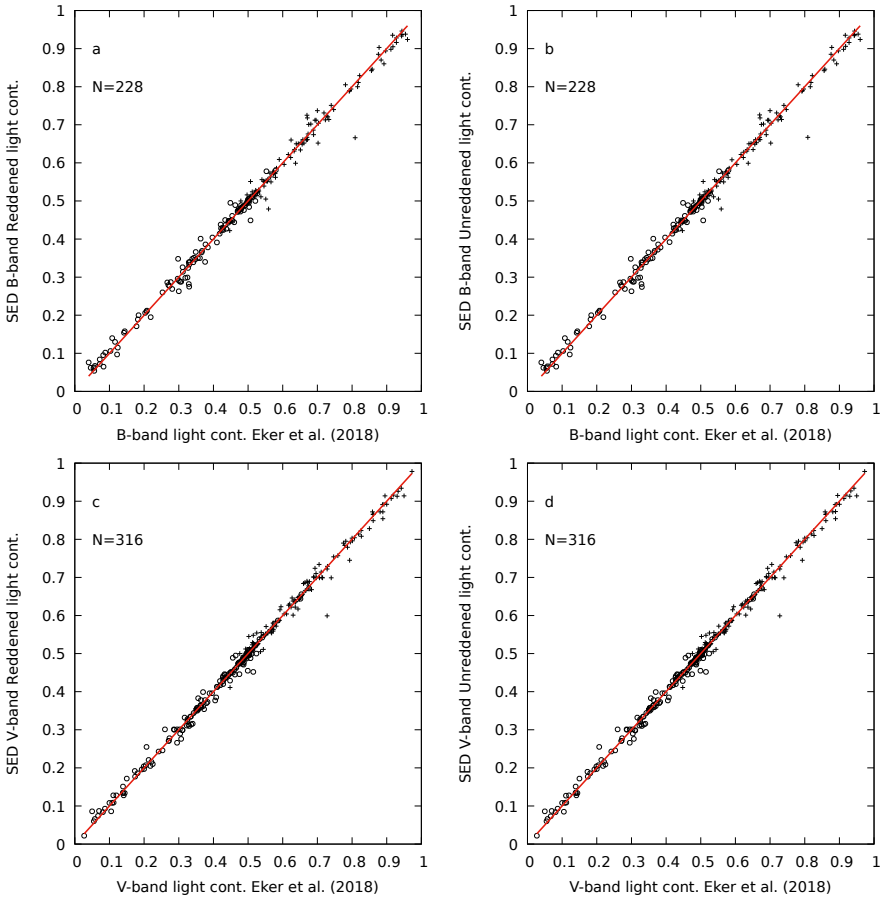

Fig. 3. Comparison of B and V passband calculated primary (+) and secondary (o) component light contributions with those listed in Eker *et al.* (2018). a and c are from reddened SED, b and d are from unreddened SED. Solid line refers to $y = x$. Note that the number of data points (N) are not the same. This is because some systems have only a V-band light ratio predicted from a V-band light curve while the rest have both B and V-band light ratios from B and V-band light curves.

served spectrum with a sufficient resolution but a spectrum represented by a Planck function with $T_{\rm eff}$ of the component. The consequence errors are expected because simplifications introduced by Planck functions make some prominent spectral features lost, thus the computed *BC* would be affected. Existence of a consequence or a zero-point error is sufficient to make a calculated *BC* non-standard.

Zero-point errors are avoided if one uses Eqs.(3) and (9), as it was claimed by IAU 2015 GAR B2 and Eker *et al.* (2021a), when computing *BC* of a component directly from $BC_V = M_{\rm bol} - M_V$. For the consequence errors, however, we claim: Unlike Eq.(1) with a simplified SED excluding certain prominent spectral features together with spectral lines, the method in this study, which uses Eq.(3) rather than Eq.(1), does not exclude any of the spectral features and lines despite using a simplified SED. This is because the total effect of all prominent features and lines on a spectrum is automatically included in through M_V in Eq.(3) where a simplified SED is needed indirectly only for estimating relative light contributions of binary components from which $M_{\rm bol}$ and M_V of the components are predicted.

Nevertheless, a test is necessary to make sure if the simplified SED provides reliable light contributions of the components. Fig. 3 compares fractional component contributions predicted in this study to a limited number of fractional light contributions in *B*- and *V*-passbands from the eclipsing light curves collected by Eker *et al.* (2020) for producing BC_V and $BC_V - T_{\rm eff}$ relation obtained from DDEB. The one-to-one correlation of almost all data is very clear. Not only component contributions from the reddened SED but also the unreddened SED of this study almost perfectly confirm the component contributions (columns 6–12, Table 2) obtained from the eclipsing binary light curves.

Fig. 3 confirms that even if a light curve of an eclipsing binary system is highly reddened because of interstellar extinction, the light ratio of components or component contributions predicted from light curve solutions are the same as the light contributions predicted by the new method using the reddened and unreddened SED of the system.

4. Calibrations of Multiband *BC* – Temperature Relations

Once *BC*s according to Eq.(3) are available (Table 4), then it is straightforward to calibrate $BC - T_{\rm eff}$ relations using $T_{\rm eff}$ of the component stars. The least-squares method is used to obtain the best-fitting curve of a calibrated $BC - T_{\rm eff}$. Fig. 4 shows the empirical standard *BC* values computed in this study and the best-fitting fourth-degree polynomials together with 1σ deviations below each panel for G, $G_{\rm BP}$ and $G_{\rm RP}$. Empirical standard $BC - T_{\rm eff}$ relations for *V*- and *B*-passbands of Johnson photometry are also produced for comparing $BC - T_{\rm eff}$ of the *V*-band by Eker *et al.* (2020). Fig. 5 shows the $BC - T_{\rm eff}$ curves for *B*- and *V*-bands.

Comparing component light contributions produced in this study to the ones from light curve solutions as in Fig. 3 is a preliminary test of the new method

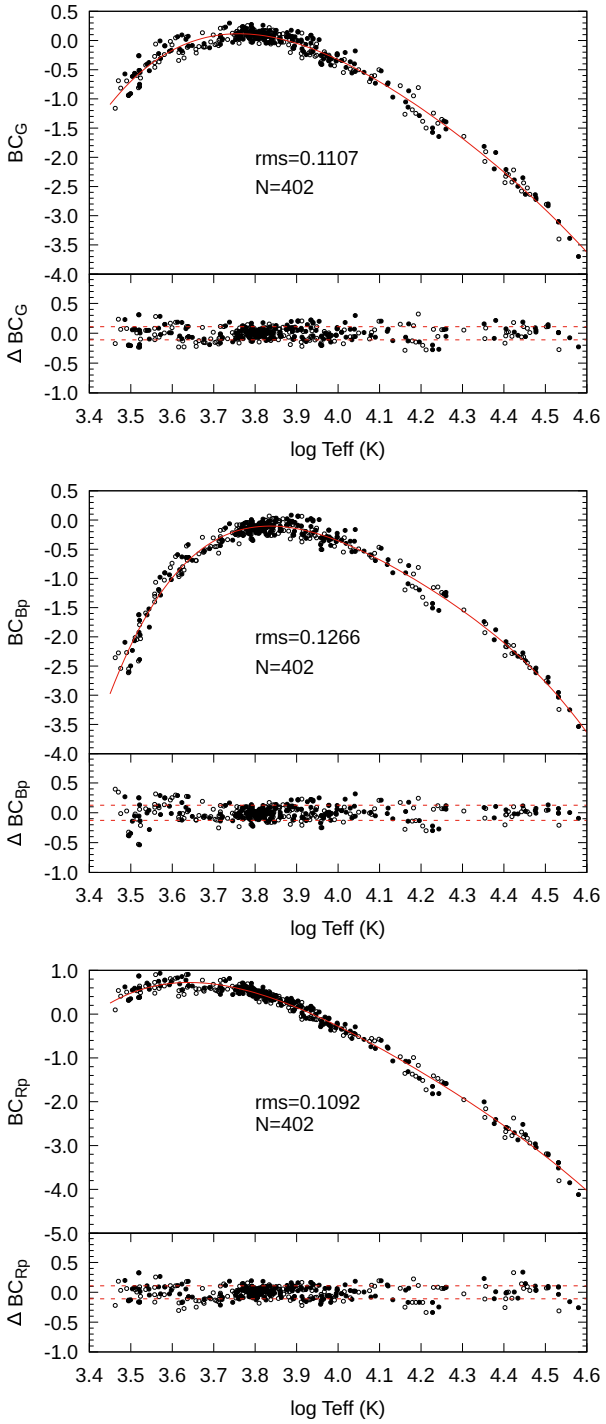

Fig. 4. Empirical Standard $BC - T_{\rm eff}$ relation for G (*top*), $G_{\rm BP}$ (*middle*) and $G_{\rm RP}$ passbands (*bottom*). The best-fitting curves (solid lines), the standard (*rms*) and 1σ deviations (dashed lines) are indicated. N is the total number of standard BC, used in the fit. Filled and empty circles refer to primary and secondary components, respectively.

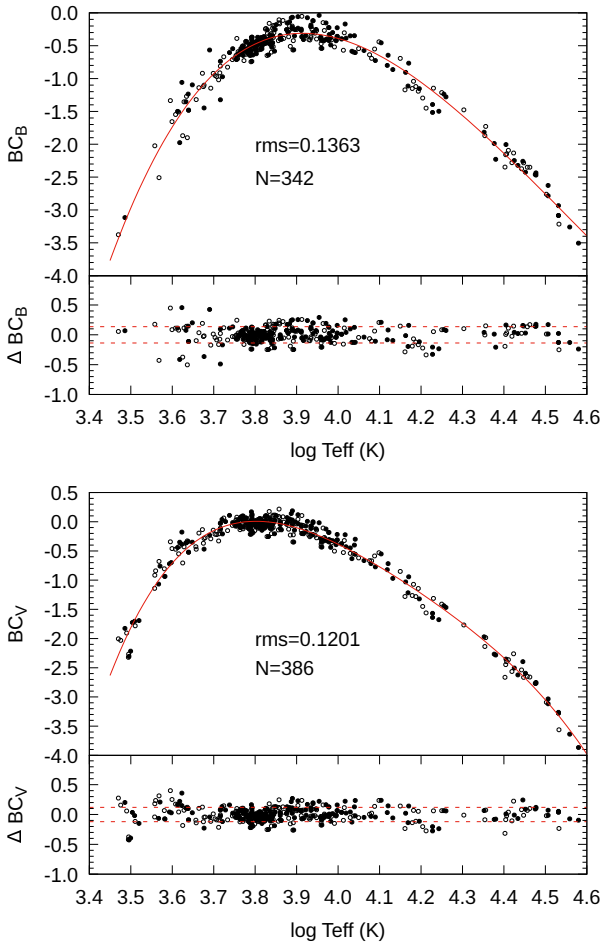

Fig. 5. Empirical standard $BC - T_{\rm eff}$ relation for B (*top*) and V-passbands (*bottom*). The best-fitting curves (solid lines), the standard (*rms*) and 1σ deviations (dashed lines) are indicated. N is the total number of standard BCs. Filled and empty circles refer to primary and secondary components, respectively.

wether reliable component contributions are produced or not. Having consistent $BC-T_{\rm eff}$ relations in all the passbands B, V, G, $G_{\rm BP}$ and $G_{\rm RP}$ is the second test of the new method, which is successful again. Successfully produced $BC-T_{\rm eff}$ relations confirm not only the validity of component light contributions but also confirm the reliability of dimming (A_ξ) provided using the new method.

Coefficients and uncertainties for the $BC-T_{\rm eff}$ functions from the least-square method are listed in Table 5 where the columns are for the photometric bands used in this study including a comparison column (column 4) of Eker *et al.* (2020). The rows are for the coefficients of the fitting polynomial, where associated errors are indicated by $\pm$ just below the value of a coefficient. The lower part of the table compares standard deviation (*rms*), correlation (R^2), and the standard BC of a main-sequence star with $T_{\rm eff} = 5772$ K (a solar twin). Maximum BC and

corresponding effective temperatures are given below the absolute and apparent magnitudes. The lowest part of the table is for indicating the range of the positive *BC* values if exist. T_1 and T_2 are the two temperatures, which make $BC = 0$. The *BC* values between T_1 and T_2 are all positive else negative. If T_1 and T_2 are not given, then all *BC* values are all negative or all positive. If only T_2 is given, then *BC* is positive for $T_{\rm eff} < T_2$, $BC = 0$ if $T_{\rm eff} = T_2$ else *BC* is negative.

Table 5 indicates $BC-T_{\rm eff}$ curve of this study has a smaller *rms* and higher correlation (R^2 value) compared to the *rms* and correlation coefficient obtained in Eker *et al.* (2020). Fig. 6a compares the $BC_V-T_{\rm eff}$ curve of this study to the $BC_V-T_{\rm eff}$ curves by Flower (1996), Eker *et al.* (2020), Mamajek (2021, private communication) and Cox (2000). *BC*s of Cox (2000) are all overestimated (more negative) compared to other *BC* displayed in the figure except Flower's (1996) toward the coolest part of the temperature scale. The *BC* values of Mamajek (2021) appear overestimated (more negative) compared to the *BC* values of Eker *et al.* (2020) for the stars hotter than 10 000 K, also for a very small range of coolest stars but the rest appears to be the same. The *BC* values of Flower (1996) deviate from the curve of Eker *et al.* (2020) and Mamajek (2021) as being bigger absolute value toward the coolest temperatures. Nevertheless, except for a limited temperature range near 10 000 K, all other *BC* values appear underestimated when compared to the standard *BC*s of this study.

Several tables exist which provide *BC*s in different photometric passbands including Gaia photometry (Martins and Plez 2006, Jordi *et al.* 2010 and Pedersen *et al.* 2020) as a function of atmospheric parameters $T_{\rm eff}$, $\log g$, ζ or [Fe/H] and are commonly used to derive isochrones in different colors, Girardi *et al.* (2002) is one example. First, Andrae *et al.* (2018) combined BC_G of various atmospheric parameters ($\log g$, ζ, metallicity) and produced a single $BC_G-T_{\rm eff}$ relation for the main-sequence stars having effective temperatures (3300–8000 K). Later, Pedersen *et al.* (2020) gave the same for temperature range (10 000–30 000 K) together with other 26 filters commonly used. Fig. 6b compares empirical $BC-T_{\rm eff}$ curve in the *G*-band of this study to the *G*-band $BC-T_{\rm eff}$ curve of Andrae *et al.* (2018) and Pedersen *et al.* (2020), which appears overestimating *G*-band *BC* for the stars cooler than 6500 K and hotter than 10 000 K, respectively. Other $BC-T_{\rm eff}$ relations representing a specific ζ or [Fe/H] predicted from model atmospheres are not suitable for comparison to the empirical relations of this study.

Empirical $BC-T_{\rm eff}$ relations are not like fundamental relations, *e.g.*, Stefan-Boltzmann law. They are rather statistical relations like classical *MLR* (Eker *et al.* 2018, 2021b). They could be used only under correct conditions set statistically. Because of stellar evolution (Clayton 1968), there could be many stars with the same M but various L due to different ages, different chemical compositions and internal mixing. Therefore, in reality, there is no unique luminosity (L) for a typical main-sequence star of a given mass (M). However, with a large uncertainty covering L values of all main-sequence stars, the classical *MLR*'s may provide

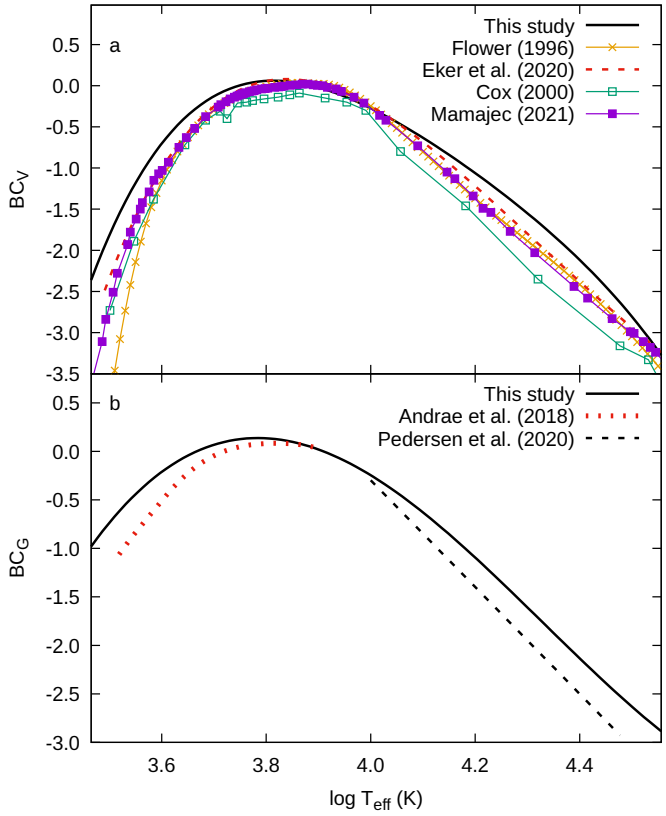

Fig. 6. Comparing $BC-T_{\rm eff}$ relations of this study to others for V (*a*) and G-bands (*b*).

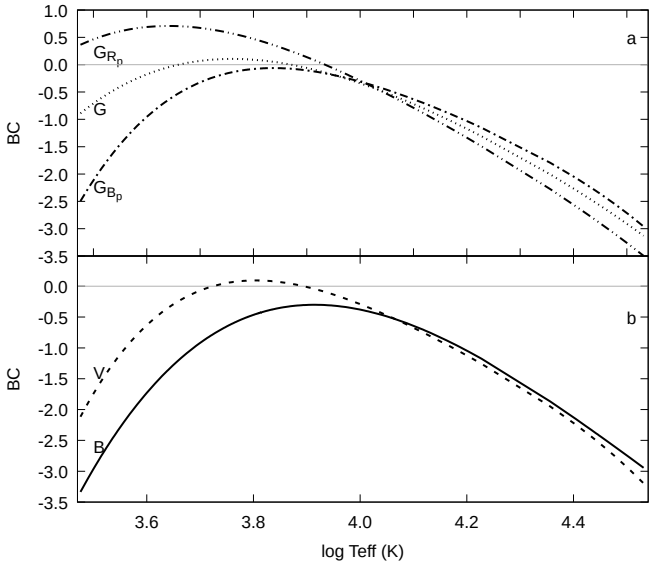

Fig. 7. Standard $BC-T_{\rm eff}$ relations in all passbands indicated on the left of each line.

T a b l e 5

Parameters for passband based *BC vs.* temperature relations

Coefficient	BC_B	BC_V	BC_V*	BC_G	$BC_{G_{\rm BP}}$	$BC_{G_{\rm RP}}$
a	−1272.43	−3767.98	−2360.69565	−1407.14	−3421.55	−1415.67
	±394.2	±288.8	±519.80058	±256.7	±293.6	±253.3
b	1075.85	3595.86	2109.00655	1305.08	3248.19	1342.38
	±394.4	±290.9	±519.47090	±258.9	±296.1	±255.4
c	−337.831	−1286.59	−701.96628	−453.605	−1156.82	−475.827
	±147.7	±109.6	±194.29038	±97.67	±111.7	±96.34
d	46.8074	204.764	103.30304	70.2338	183.372	74.9702
	±24.53	±18.32	±32.23187	±16.34	±18.68	±16.12
e	−2.42862	−12.2469	−11.5957	−4.1047	−10.9305	−4.44923
	±1.552	±1.146	±1.441	±1.023	±1.169	±1.009
rms	0.136257	0.120071	0.215	0.11068	0.126577	0.109179
R^2	0.9616	0.9789	0.941	0.9793	0.9738	0.9884
$BC_\odot$ [mag]	−0.600	0.069	−0.016	0.106	−0.134	0.567
$M_\odot$ [mag]	5.340	4.671	4.756	4.634	4.874	4.173
$m_\odot$ [mag]	−26.232	−26.901	−26.816	−26.938	−26.698	−27.399
$BC_{\rm max}$ [mag]	−0.301	0.094	0.095	0.106	−0.062	0.709
$T_{\rm max}$ [K]	8222	6397	6897	5715	6879	4345
T_1 [K]	–	5300	5859	4565	–	–
T_2 [K]	–	7830	8226	7420	–	8590

*: Eker *et al.* (2020)

Parameters have the form $BC_\xi = a + b \times (\log T_{\rm eff}) + c \times (\log T_{\rm eff})^2 + d \times (\log T_{\rm eff})^3 + e \times (\log T_{\rm eff})^4$ (Figs. 4 and 5). For the calculation of passband based solar absolute magnitudes, solar absolute bolometric magnitude is adopted to be $M_{\rm bol,\odot} = 4.74$ and the $BC_\odot$ refers to $T_{\rm eff,\odot} = 5772$ K. The relations are valid in the temperature range of 2900–38 000 K.

only a mean L for a typical main-sequence star of a given M. The same is true that the $BC-T_{\rm eff}$ relations may provide only a mean or a typical BC for a typical main-sequence star of a given typical $T_{\rm eff}$.

Therefore, it is an astrophysical interest to have a table indicating typical $T_{\rm eff}$ and typical BC of main-sequence stars. Table 6 is the extension of an original table given by Eker *et al.* (2018) and Eker *et al.* (2020), where typical fundamental astrophysical parameters of main-sequence stars are presented with BC, $(B-V)_0$ and M_V as a function of typical effective temperatures associated with the spectral types. Table 6, here, is kept short to contain only spectral types, typical $T_{\rm eff}$ and mean BCs and intrinsic colors of nearby Galactic main-sequence stars with $0.008 < {\rm Z} < 0.040$ for the bands B, V, G, $G_{\rm BP}$ and $G_{\rm RP}$.

An interesting feature of multiband $BC-T_{\rm eff}$ relations would be revealed if the BC values on Table 6 are plotted on a single frame (Fig. 7) as a function of effective temperature. It is not a surprise to see $BC-T_{\rm eff}$ relations of Gaia passbands (Fig. 7a) cut each other at a common point near $\approx 10\,000$ K ($\log T_{\rm eff} = 4$). This must be due

T a b l e 6

Mean bolometric corrections and intrinsic colors of nearby main-sequence stars as a function of typical effective temperature and spectral types having metallicities $0.008 < Z < 0.040$ for the passbands B, V, G, $G_{\rm BP}$ and $G_{\rm RP}$

		From Table 5							From Table 8	
SpT	Teff (K)	BC_B [mag]	BC_V [mag]	BC_G [mag]	$BC_{G_{\rm BP}}$ [mag]	$BC_{G_{\rm RP}}$ [mag]	$(G-G_{\rm RP})_0$ [mag]	$(G_{\rm BP}-G_{\rm RP})_0$ [mag]	$(G_{\rm BP}-G_{\rm RP})_0$ [mag]	$(B-V)_0$ [mag]
O7	35810	−3.088	−3.399	−3.291	−3.150	−3.671	−0.380	−0.521	−0.562	−0.364
O8	33963	−2.941	−3.192	−3.126	−2.957	−3.492	−0.367	−0.536	−0.543	−0.352
O9	32211	−2.795	−2.997	−2.965	−2.775	−3.319	−0.354	−0.544	−0.525	−0.340
B0	29512	−2.556	−2.700	−2.709	−2.497	−3.042	−0.334	−0.545	−0.493	−0.320
B1	25119	−2.127	−2.218	−2.266	−2.045	−2.561	−0.296	−0.516	−0.432	−0.279
B2	21135	−1.690	−1.769	−1.827	−1.626	−2.079	−0.252	−0.453	−0.359	−0.231
B3	18408	−1.364	−1.446	−1.501	−1.327	−1.714	−0.212	−0.387	−0.295	−0.190
B5	15136	−0.955	−1.029	−1.076	−0.946	−1.222	−0.146	−0.276	−0.194	−0.123
B6	13964	−0.808	−0.869	−0.914	−0.803	−1.029	−0.115	−0.226	−0.148	−0.093
B7	13032	−0.694	−0.737	−0.782	−0.687	−0.868	−0.086	−0.181	−0.106	−0.065
B8	12023	−0.576	−0.591	−0.636	−0.560	−0.685	−0.049	−0.125	−0.053	−0.031
B9	10666	−0.436	−0.389	−0.437	−0.390	−0.425	0.012	−0.035	0.032	0.026
A0	9886	−0.371	−0.274	−0.323	−0.297	−0.269	0.055	0.028	0.093	0.067
A1	9419	−0.340	−0.206	−0.257	−0.243	−0.173	0.084	0.070	0.135	0.095
A2	9078	−0.322	−0.158	−0.209	−0.206	−0.102	0.107	0.104	0.168	0.118
A3	8750	−0.309	−0.113	−0.164	−0.173	−0.033	0.130	0.140	0.202	0.142
A5	8222	−0.301	−0.045	−0.094	−0.125	0.078	0.172	0.204	0.266	0.185
A6	7980	−0.303	−0.016	−0.064	−0.107	0.130	0.194	0.237	0.298	0.209
A7	7745	−0.308	0.009	−0.036	−0.091	0.179	0.215	0.271	0.332	0.233
A8	7534	−0.317	0.030	−0.012	−0.079	0.224	0.236	0.304	0.365	0.257
F0	7161	−0.343	0.062	0.027	−0.066	0.302	0.275	0.367	0.427	0.303
F1	6966	−0.363	0.075	0.045	−0.062	0.342	0.297	0.404	0.466	0.331
F2	6792	−0.384	0.084	0.059	−0.062	0.377	0.318	0.440	0.501	0.357
F3	6637	−0.406	0.089	0.071	−0.064	0.408	0.337	0.473	0.535	0.382
F5	6397	−0.447	0.094	0.086	−0.073	0.455	0.369	0.529	0.591	0.429
F6	6310	−0.464	0.093	0.091	−0.078	0.472	0.381	0.550	0.613	0.447
F7	6223	−0.483	0.092	0.095	−0.084	0.488	0.393	0.573	0.636	0.465
F8	6152	−0.499	0.091	0.098	−0.090	0.501	0.403	0.591	0.655	0.481
G0	6026	−0.530	0.086	0.102	−0.102	0.524	0.422	0.626	0.690	0.510
G1	5957	−0.548	0.082	0.104	−0.110	0.536	0.433	0.646	0.710	0.526
G2	5888	−0.567	0.078	0.105	−0.118	0.548	0.443	0.667	0.730	0.543
G3	5848	−0.579	0.075	0.105	−0.124	0.555	0.450	0.679	0.743	0.554
G5	5741	−0.612	0.065	0.106	−0.140	0.573	0.467	0.713	0.776	0.582
G6	5689	−0.629	0.060	0.106	−0.148	0.581	0.476	0.730	0.793	0.596
G7	5649	−0.642	0.055	0.105	−0.155	0.588	0.483	0.743	0.806	0.607
G8	5559	−0.674	0.044	0.104	−0.172	0.602	0.498	0.774	0.837	0.633
K0	5248	−0.801	−0.010	0.090	−0.247	0.645	0.556	0.892	0.951	0.729
K1	5070	−0.888	−0.054	0.075	−0.302	0.666	0.591	0.969	1.028	0.788
K2	4898	−0.982	−0.106	0.056	−0.366	0.683	0.628	1.049	1.102	0.846
K3	4732	−1.085	−0.167	0.031	−0.439	0.696	0.665	1.135	1.177	0.902
K5	4345	−1.375	−0.362	−0.053	−0.660	0.709	0.762	1.368	1.365	1.025
M0	3802	−1.939	−0.803	−0.258	−1.138	0.666	0.924	1.804	1.659	1.193
M1	3648	−2.143	−0.977	−0.341	−1.323	0.636	0.978	1.959	1.750	1.240
M2	3499	−2.363	−1.174	−0.435	−1.528	0.598	1.033	2.126	1.845	1.286
M3	3350	−2.610	−1.402	−0.545	−1.765	0.547	1.092	2.312	1.947	1.331
M4	3148	−2.991	−1.770	−0.722	−2.143	0.457	1.179	2.600	2.111	1.393
M5	2999	−3.314	−2.094	−0.879	−2.473	0.370	1.249	2.843	2.264	1.439

to using the Vega system of magnitudes, which assumes zero intrinsic colors for a hypothetical star of A0V spectral type with an effective temperature 10 000 K. The Vega system of magnitudes uses Vega as the standard star and assumes that all intrinsic colors of Vega are equal to 0. While Vega is classified as an A0V star, its effective temperature is 9600 K while its apparent brightness is $V = 0.03$ mag. The crossing point of the $BC-T_{\rm eff}$ relations of Johnson *B*, *V* occurring erroneously at a higher temperature (Fig. 7b) indicates lower precision and accuracy of Johnson magnitudes with respect to Gaia magnitudes used in this study. This is not a surprise because the total *B* and *V* brightness of DDEB systems are collected from various sources (see Table 1) unlike Gaia magnitudes, which are taken from a single source, EDR3. The maximum *BC* and/or ranges of positive *BC* values given in Table 5 are visualized in Fig. 7.

5. How to Improve Standard Luminosities

Improving the accuracy of standard L could be achieved in two ways. One way is to improve the accuracy of existing standard $BC-T_{\rm eff}$ relations and the second way is to increase the diversity of the standard $BC-T_{\rm eff}$ relations. The former way is already achieved by calibrating multiband standard $BC-T_{\rm eff}$ relations using the most accurate stellar astrophysical data available. The improved relations and their related statistics are given in Table 5. A user would produce a standard L of a star almost twice more accurate now if he/she uses $BC_V-T_{\rm eff}$ relation of this study rather than $BC_V-T_{\rm eff}$ relation of Eker *et al.* (2020) if propagated uncertainty of M_V of the star is dominated by relative parallax error $\left(\frac{\sigma_\varpi}{\varpi}\right)$ and if it is $\sigma_\varpi/\varpi \ll 5.5$ per cent. This is because the standard deviation of the $BC_V - T_{\rm eff}$ curve of this study is reduced to $SD = 0.12$ mag implying 11.05 per cent for $\Delta L/L$ if M_V is errorless, while it was $SD = 0.215$ mag (see Table 5) implying 19.8 per cent for $\Delta L/L$ correspondingly. Otherwise (if $\sigma_\varpi/\varpi \gg 5.5$ per cent), the uncertainty of computed L would naturally be dominated by the parallax error. Then, the propagated uncertainty of the standard L would have been much bigger ($\Delta L/L \gg 11.05$ per cent).

The standard deviation of a $BC_V - T_{\rm eff}$ curve determines the limiting accuracy of the standard L (Eker *et al.* 2021b). Therefore, Table 5 implies that a user can obtain a standard L with an error as small as 12.5 per cent, 11.05 per cent, 10.2 per cent, 11.7 per cent, or 10.05 per cent correspondingly if he/she uses one of the $BC - T_{\rm eff}$ relations at *B*, *V*, G, $G_{\rm BP}$, or $G_{\rm RP}$ photometric bands, respectively. However, if $\sigma_\varpi/\varpi \gg 6.3$ per cent, 5.5 per cent, 5.1 per cent, 5.8 per cent or 5.02 per cent, in accord with the photometric bands, the standard error of the L is bigger. At the limit, when the uncertainty of M_V dominates over the uncertainty of *BC* and the distance errors dominate over brightness and extinction errors, it becomes twice the relative error of the parallax according to the formulation of Eker *et al.* (2021b).

Providing independent $BC-T_{\rm eff}$ relations at B, V, G, $G_{\rm BP}$- or $G_{\rm RP}$-passbands determined independently by the least-squares method from the independent observational photometric and astrometric data of DDEB, which are known to provide the most accurate stellar astrophysical parameters, Table 5 allowed us to investigate the second way of improving the accuracy of a standard L. One does not need to calculate the actual value of the standard L for speculating about its relative uncertainty ($\Delta L/L$) if it comes from a single $BC-T_{\rm eff}$ relation. Similar speculations, however, are not possible in the second way of improving. Calculation of actual L from each of the $BC-T_{\rm eff}$ relations is needed.

Then, there are many standard L values for a star representing each of the photometric bands, like many independent measurements of a quantity. However, we prefer not to calculate many different standard L for a star and then take an average. Instead, we prefer to predict five different $M_{\rm bol}$ together with their associated uncertainty propagated from the uncertainty of M_ξ, and the uncertainty of BC_ξ (Table 5) first. Then, we combine them according to

$$M_{\rm bol} = \frac{1}{N}\sum_{i}^{N} M_{{\rm bol},i} \tag{10}$$

to obtain a single $M_{\rm bol}$ for a star, where $M_{{\rm bol},i} = M_i + BC_i$, provided with $i = B$, V, G, $G_{\rm BP}$, and $G_{\rm RP}$ passbands. N is a number between 2 (if $M_{\rm bol}$ is predicted from B, V only) and 5 (if $M_{\rm bol}$ is predicted from all the passbands) because some systems do not have total apparent brightness measured at certain photometric bands. At last, the most improved standard L of a star is predicted directly from its mean $M_{\rm bol}$ value according to Eq.(9). To estimate its relative uncertainty ($\Delta L/L$), we preferred to calculate a standard error for the $M_{\rm bol}$ first and then propagate it to the standard L. A similar approach of using an average bolometric magnitude calculated based on several different photometric passbands to derive L was used by Pedersen *et al.* (2020) to derive L of B dwarfs, but for apparent instead of absolute bolometric magnitudes.

Predicted (from photometry) and calculated (from R and $T_{\rm eff}$) L of the sample stars in this study are compared in Fig. 8a. A very high correlation ($R^2 > 0.999$) between the predicted and calculated luminosities is seen clearly. Fig. 8b compares histogram distributions of their uncertainties. Uncertainties of the predicted L have a sharp well-defined peak at 2 per cent with a smaller dispersion, while the uncertainties of the calculated L have a fussy peak at 8 per cent with a much wider dispersion. Fig. 8 shows that a prominent improvement in predicting a standard L of a star occurs if all the existing independent $BC-T_{\rm eff}$ relations are used according to the method introduced in this study. The improvement is remarkable and real (not speculative) that there is a method, now, which could provide a standard luminosity of a star more accurate than the classical method using observed radii and effective temperatures according to the Stefan-Boltzmann law.

Table 7

Component bolometric magnitudes and luminosities of DDEB in B, V, G, $G_{\rm BP}$ and $G_{\rm RP}$ passbands

Order	Name	pri/sec	$M_{\rm bol}(B)$ [mag]	err [mag]	$M_{\rm bol}(V)$ [mag]	err [mag]	$M_{\rm bol}(G)$ [mag]	err [mag]	$M_{\rm bol}(G_{\rm BP})$ [mag]	err [mag]	$M_{\rm bol}(G_{\rm RP})$ [mag]	err [mag]	$\langle M_{\rm bol}\rangle$ [mag]	Mean err [mag]	log $\langle L/L_\odot\rangle$	$\frac{\Delta L}{L}$ [%]	log $(L/L_\odot)$(SB)	$\frac{\Delta L}{L}$ [%]
1	V421 Peg	p	2.760	0.143	2.825	0.124	2.722	0.115	2.789	0.133	2.713	0.111	2.762	0.021	0.791	1.924	0.796	5.655
2	V421 Peg	s	3.312	0.143	3.383	0.124	3.284	0.115	3.349	0.133	3.271	0.111	3.320	0.021	0.568	1.919	0.577	8.146
3	DV Psc	p	6.499	0.142	6.741	0.124	6.751	0.115	6.789	0.134	6.757	0.112	6.707	0.053	−0.787	4.857	−0.780	8.789
4	DV Psc	s	8.051	0.142	8.115	0.124	8.317	0.115	8.160	0.134	8.369	0.112	8.202	0.061	−1.385	5.580	−1.391	7.832
5	MU Cas	p	−2.240	0.164	−2.208	0.148	−2.329	0.140	−2.255	0.155	−2.293	0.137	−2.265	0.021	2.802	1.943	2.875	13.768
6	MU Cas	s	−2.060	0.164	−2.021	0.148	−2.145	0.140	−2.070	0.155	−2.108	0.137	−2.081	0.021	2.728	1.950	2.800	13.423
7	TYC 4019-3345-1	p	1.687	0.145	1.764	0.127	1.549	0.118	1.601	0.136	1.601	0.115	1.640	0.038	1.240	3.496	1.184	15.498
8	TYC 4019-3345-1	s	1.687	0.145	1.764	0.127	1.549	0.118	1.601	0.136	1.601	0.115	1.640	0.038	1.240	3.496	1.184	27.114
9	YZ Cas	p	0.540	0.145	0.642	0.125	0.562	0.115	0.591	0.133	0.591	0.112	0.585	0.017	1.662	1.569	1.674	5.117
10	YZ Cas	s	3.382	0.145	3.533	0.125	3.469	0.115	3.505	0.133	3.466	0.112	3.471	0.025	0.508	2.340	0.553	13.983
...	...	...	...	...	...	...	...	...	...	...	...	...	...	...	...	...	...	...
409	IT Cas	p	3.174	0.145	3.261	0.131	3.153	0.116	3.214	0.134	3.144	0.113	3.189	0.022	0.620	1.988	0.608	7.053
410	IT Cas	s	3.220	0.145	3.307	0.131	3.200	0.116	3.261	0.134	3.191	0.113	3.236	0.022	0.602	1.988	0.590	8.500
411	BK Peg	p	2.926	0.148	2.981	0.125	2.846	0.115	2.925	0.133	2.827	0.112	2.901	0.028	0.736	2.617	0.738	5.487
412	BK Peg	s	3.537	0.148	3.591	0.125	3.454	0.115	3.534	0.133	3.436	0.112	3.510	0.029	0.492	2.645	0.493	2.990
413	AP And	p	3.796	0.154	3.879	0.151	3.724	0.116	3.805	0.134	3.713	0.112	3.783	0.030	0.383	2.772	0.406	9.194
414	AP And	s	3.911	0.154	3.996	0.151	3.843	0.116	3.923	0.134	3.831	0.112	3.901	0.030	0.336	2.750	0.360	9.280
415	AL Scl	p	−1.414	0.163	−1.361	0.147	−1.405	0.139	−1.368	0.154	−1.409	0.136	−1.391	0.011	2.453	1.032	2.504	10.783
416	AL Scl	s	1.659	0.163	1.686	0.147	1.658	0.139	1.696	0.154	1.627	0.136	1.665	0.012	1.230	1.116	1.299	14.269
417	V821 Cas	p	0.865	0.146	0.929	0.126	0.819	0.115	0.847	0.133	0.846	0.112	0.861	0.018	1.552	1.694	1.574	17.193
418	V821 Cas	s	2.365	0.146	2.440	0.126	2.332	0.115	2.365	0.133	2.350	0.112	2.371	0.018	0.948	1.688	0.979	18.872

Full versions of Tables 3 and 4 are available form the *Acta Astronomica Archive* (see cover page)

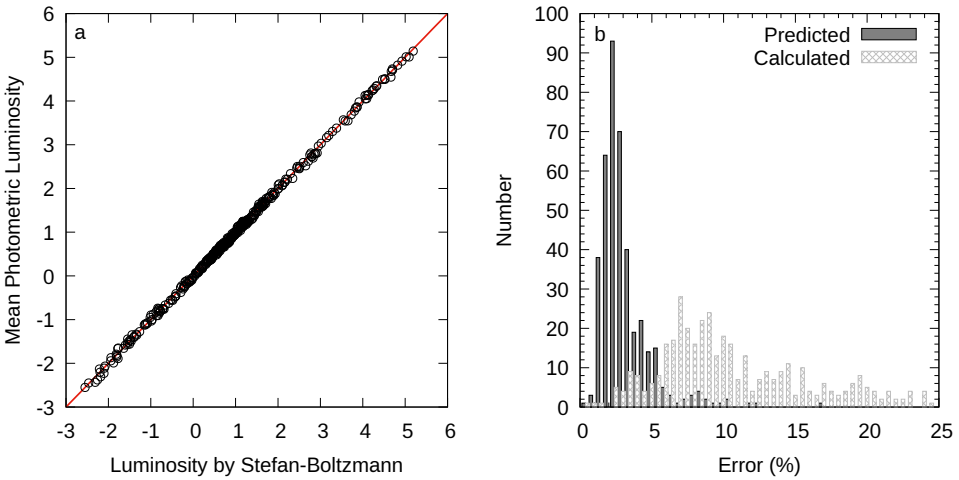

Fig. 8. a) Comparing predicted (from photometry) and calculated (from R and $T_{\rm eff}$) L of the sample stars. b) Histogram distribution of the uncertainties associated with predicted (dark) L is compared to the histogram distribution of the uncertainties associated with calculated (gray) L.

We summarize the data produced by the method used in this study in Table 7. The columns are self-explanatory to show order, system name, the component (primary or secondary) in the first three columns. Then next ten columns are reserved for the predicted $M_{\rm bol}$ values from its definition ($M_{\rm bol} = M_\xi + BC_\xi$) and associated propagated errors at B, V, G, $G_{\rm BP}$, and $G_{\rm RP}$ passbands. Then, the combined (mean) $M_{\rm bol}$ and its standard error are provided in columns 14 and 15. The logarithm of the predicted L in solar units and its relative uncertainty are listed in columns 16 and 17. The last two columns are for the calculated L in solar units and their relative uncertainty. Fig. 8 is produced from the last four columns of Table 7. Therefore, the last four columns are ideal for a reader who is interested in comparing actual numerical values of the predicted and computed L and to see how small the relative errors of the predicted L are compared to the errors of the computed L.

6. Discussions

6.1. The Sun and a Solar Twin for Testing

In a first thought, one may think the Sun is not a good candidate for testing how good its luminosity would be predicted according to the method described in this study because it is the reference star that IAU 2015 GAR B2 used to determine the zero point constant of the bolometric magnitude scale $C_{\rm bol} = 71.197\,425\ldots$ mag from $L = 3.8275(\pm 0.0014) \times 10^{26}$ W and $M_{{\rm bol},\odot} \cong 4.739\,996\ldots$ mag. The BC values (-0.600, 0.069, 0.106, -0.134, 0.567 respectively at B, V, G, $G_{\rm BP}$ and $G_{\rm RP}$) given in Table 5, which are marked with $_\odot$ symbol, should not be understood as the BC of the Sun. They are the predicted BC values for a typical main-sequence star having $T_{\rm eff} = 5772$ K. Consequently, absolute and apparent magnitudes given

in Table 5 just below those *BC* values are typical absolute and apparent magnitudes if this star is replaced as the Sun. Now the question: is it possible to estimate the luminosity of the Sun just from its effective temperature ($T_{\rm eff,\odot} = 5772$ K) using the *BC* given in Table 5? To proceed toward this aim, one needs apparent magnitudes and distance as in the other stars used in this study.

While apparent magnitudes in the Gaia passbands for the Sun could be calculated using a measured/calculated solar composite spectrum (Willmer 2018), one for sure cannot find measured Gaia apparent magnitudes. However, it is possible to find a measured $V_\odot = -26.76 \pm 0.03$ mag value (Torres 2010). Same and slightly different (in the second digit after the decimal) values seem to be preferred by various authors (see the references in Torres 2010, and Eker *et al.* 2021b). Astronomers handbook "Allen's Astrophysical Quantities" (Cox 2000) gives it 0.01 mag dimmer, where apparent and absolute magnitudes of the Sun in *U, B, V, R, I*, and *K*-bands could be found. Taking $(B-V)_\odot = 0.65$ mag, one can start from $V_\odot = -26.76$ mag and $B_\odot = -26.11$ mag and continue predicting the solar luminosity together with its uncertainty by applying the method described in this study. Here, we assume *B* and *V* apparent magnitudes of the Sun have the same uncertainty (± 0.03 mag).

No interstellar extinction for the Sun and because its distance is also known with a great precision compared to other stars, only the observational uncertainty $\Delta V \approx \Delta B \approx 0.03$ mag propagates to the solar absolute magnitudes: $M_{V,\odot} = 4.812 \pm 0.03$ mag, and $M_{B,\odot} = 5.462 \pm 0.03$ mag. Using the *BC* and *rms* values (Table 5) for a typical main-sequence star with $T_{\rm eff} = 5772$ K, the predicted bolometric magnitudes of the Sun would be $M_{\rm bol,\odot}(1) = 4.881 \pm 0.136$ mag and $M_{\rm bol,\odot}(2) = 4.862 \pm 0.12$ mag, respectively from its *V* and *B* magnitudes. After combining them by taking a simple average $M_{\rm bol,\odot} = 4.872$ mag. The differences from the mean indicate an ± 0.095 mag uncertainty. At last, using Eq.(9), the predicted solar luminosity is $L_P(\odot) = 3.39 \times 10^{26}$ W, and the relative uncertainty is $\Delta L/L \approx 8.7$ per cent.

Comparing this value to the nominal Solar luminosity $L = 3.838 \times 10^{26}$ W, one can see how successful the method is. A luminosity, which is about 11.7 per cent smaller than actual $\rm L_\odot$, is predicted. A single channel prediction from $M_{\rm bol,\odot}(1)$ or $M_{\rm bol,\odot}(2)$, would have given us a prediction with a relative error of 12.5 per cent or 11.05 per cent respectively. All predicted L values agree to the read L within the error limits estimated.

6.2. A Solar Twin for a Test

The primary of HP Aur system with a mass $M = 0.9543 \pm 0.0041$ $\rm M_\odot$, a radius $R = 1.0278 \pm 0.0042$ $\rm R_\odot$, and an effective temperature $T_{\rm eff} = 5810 \pm 120$ K (Lacy *et al.* 2014) could be considered as a solar twin. According to the Stefan-Boltzmann law, its luminosity is $L = 1.084$ $\rm L_\odot = 4.162 \times 10^{26}$ W. Propagation of the observational uncertainties shows its relative error ($\Delta L/L$) would be about

8.302 per cent. Now the question is: Using the method of this study, how accurately would its luminosity be predicted?

Its apparent brightnesses are $V = 11.489 \pm 0.07$, $G = 11.283 \pm 0.003$, $G_{\rm BP} = 11.628 \pm 0.004$, $G_{\rm RP} = 10.761 \pm 0.004$ mag. According to simplified SED, the primary contributes 75.7 per cent of the total light radiated by the system in *V*, 75 per cent in *G*, 76.5 per cent in $G_{\rm BP}$ and 72.9 percent in $G_{\rm RP}$. The simplified SED also implies $A_V = 0.335$ mag, $A_G = 0.298$ mag, $A_{G_{\rm BP}} = 0.366$ mag, and $A_{G_{\rm RP}} = 0.207$ mag as the interstellar dimming. Parallax of the system is 5.2432 ± 0.0306 mas. Consequently, its absolute magnitudes are $M_V = 4.753 \pm 0.033$, $M_G = 4.583 \pm 0.033$, $M_{G_{\rm BP}} = 4.860 \pm 0.042$, and $M_{G_{\rm RP}} = 4.152 \pm 0.024$ mag. Table 5 gives $BC_V = 0.072 \pm 0.12$, $BC_G = 0.106 \pm 0.11$, $BC_{G_{\rm BP}} = -0.129 \pm 0.13$, and $BC_{G_{\rm RP}} = 0.562 \pm 0.11$ mag. Here, we notice that the errors in *BC* values are bigger than errors in filter based absolute magnitudes. Thus, they could be ignored. That is, *BC* errors would be the dominant factor when calculating the uncertainty of its bolometric absolute magnitudes. This means if single passband used in predicting its L, the relative error of its L ($\Delta L/L$) will not be smaller than 10 per cent.

According to Eq.(3), the $M_{\rm bol}$ are calculated as 4.824 mag, 4.688 mag, 4.73 mag, and 4.713 mag, respectively at four photometric bands. At last, one obtains a mean $M_{\rm bol} = 4.739 \pm 0.03$ mag for the solar twin, where its uncertainty is assumed to be the standard error by definition. After computing its L using Eq.(9), $L = 3.831 \times 10^{26}$ W is found. At last its uncertainty ± 0.03 translates to $\Delta L/L \approx 2.5$ per cent.

Predicted and calculated L for the primary of HP Aur agree to each other within the error limits. The calculated luminosity from R and $T_{\rm eff}$ using the Stefan–Boltzmann law seems to be overestimated. The predicted standard $L = 3.831 \times 10^{26}$ W appears more reliable because of its predicted uncertainty. At last, it can be concluded that the method of computing standard L of stars using multiband photometry and $BC - T_{\rm eff}$ relations involving SED is very successful in predicting luminosities much more accurately than the direct method using observed R and $T_{\rm eff}$. Using four $BC - T_{\rm eff}$ curves ended up predicting a standard L at least four times more accurately than in the case if one uses only one of the $BC - T_{\rm eff}$ relations existing.

6.3. Standard or Non-Standard

What makes *BC*s (and $BC_V - T_{\rm eff}$ relation) of this study standard? What makes *BC*s of Cassagrande and VandenBerg (2018), Cox (2020), Andrae *et al.* (2018), and Mamajek's personal online *BC* Table accessible on the internet* non-standard?

In the first look, IAU 2015 GAR B2 was issued only for solving the long-lasting problem of arbitrariness attributed to the zero point of bolometric magnitudes. However, the arbitrariness of the bolometric magnitude scale is not inde-

*www.pas.rochester.edu/∼emamajek/EEM_dwarf_UBVIJHK_colors_Teff.txt

pendent of the arbitrariness of the *BC* scale according to Eq.(3). Articles such as Cassagrande and VandenBerg (2018), Andrae *et al.* (2018), which are still defending the arbitrariness of the *BC* scale, cause confusion.

Eker *et al.* (2021a) have shown that fixing the zero point of the bolometric magnitude scale also fixes the zero point of the bolometric correction scale. To avoid *BC* determinations with different zero points, Eker *et al.* (2021a) have defined the concept of standard *BC*. The standard *BC* is not only for the *V*-band, the definition covers all bands of all photometric systems. Eker *et al.* (2021b) explained how to recognize non-standard *BC* values.

Briefly, using Eq.(9) with a definite $C_{\rm bol}$ makes the computed $M_{\rm bol}$ unique. Since stellar absolute magnitudes at well-defined passbands of various photometric systems are also unique (absolute magnitude of a star cannot have two or more values for a specified band), the product of Eq.(3) was defined as the standard *BC* because subtracting a unique number from another unique number is also unique.

The nominal value of $C_{\rm bol} = 71.197\,425\ldots$ corresponds to the nominal values of $M_{\rm bol,\odot} = 4.74$ mag (a rounded value, the true value is 4.739 996 ...) and $\mathrm{L}_\odot = 3.828x10^{26}$ W, thus $C_{\rm bol} = M_{\rm bol,\odot} + 2.5\log \mathrm{L}_\odot$ (see IAU 2015 GAR B2, Eker *et al.* (2021ab). Consequently, using a different $C_{\rm bol}$ than the nominal $C_{\rm bol}$ in Eq.(9) or using a non-nominal value of $M_{\rm bol,\odot}$ or $\mathrm{L}_\odot$ in the following equation:

$$M_{\rm bol} = M_{\rm bol,\odot} - 2.5\log\frac{L}{\mathrm{L}_\odot} \tag{11}$$

is sufficient to make a computed *BC* non-standard. Moreover, a *BC* is also not standard if it is computed through Eq.(1) with an arbitrary C_2,

Cassagrande and VandenBerg (2018) used $M_{\rm bol,\odot} = 4.75$ mag for the absolute bolometric magnitude for the Sun rather than the nominal value $M_{\rm bol,\odot} = 4.74$ mag suggested by (IAU 2015 GAR B2). On the other hand, the *BC*s of Cox (2000) are also not standard because the nominal $M_{\rm bol,\odot} = 4.74$ mag was used together with a non-nominal $L_\odot = 3.845 \times 10^{26}$ W corresponding to a non-nominal $C_{\rm bol}$ (see Eker *et al.* 2021b). Despite using the nominal values $M_{\rm bol,\odot}$ or $L_{\rm bol,\odot}$, the *BC* values of Andrae *et al.* (2018) are also not standard. This is because Andrae *et al.* (2018) preferred to use Eq.(1) with an assumed arbitrary C_2 when computing *BC* values for the Gaia photometric passbands. A slightly different case seems to have occurred on the *BC* tables given by Cox (2000), who took the arbitrariness of C_2 granted. Consequently, to be consistent with the paradigm, "bolometric corrections must be negative" (see page 381 of Cox 2000), the zero point of the *BC* scale was set to make all *BC*s negative. This is the second reason why *BC* values of Cox (2000) are not standard.

Eker *et al.* (2021a) have shown that the zero point constant in Eq.(1) has different values at different filters such: $C_2 = C_{\rm bol} - C_\xi$, where C_ξ is the zero point for a passband, thus C_2 is also not arbitrary but has a definite value. Although C_2 appears like an integration constant in Eq.(1), actually it is not an integration constant or algebraic sum of integration constants required by integrals appearing in Eq.(1).

It is well known that definite integrals do not take constants. Therefore, C_2 must be a constant imposed by the absolute photometry, such as

$$M_\xi = -2.5 \log L_\xi + C_\xi. \tag{12}$$

Subtracting this from Eq.(9), which is imposed by Eq.(3), gives Eq.(1), where the definite integrals are for producing the surface fluxes of the star for the bolometric: $f_{\rm bol} = \int_0^\infty f_\lambda \, {\rm d}\lambda$ and for a photometric band $f_\xi = \int_0^\infty S_\lambda(\xi) f_\lambda \, {\rm d}\lambda$. The definite integrals do not take constants, but the absolute photometry (Eqs. 9 and 12) requires $C_2 = C_{\rm bol} - C_\xi$.

Since the value of $C_{\rm bol}$ was unknown before IAU 2015 GAR B2, and no telescope or a detector exists to observe $M_{\rm bol}$, it was natural to assume both $C_{\rm bol}$ and C_2 arbitrary. Therefore, authors such as Cox (2000), and Pecaut and Mamajek (2013) have excuse to assume the *BC* scale is arbitrary and then impose a personal condition to set up a private absolute scale. Cox (2000) took $BC_V = 0$ for F2 supergiants and Mamajek (2021) uses $BC_V = -0.085$ mag for a G2 main-sequence star in his online *BC* table to set up a private zero point for the *BC* scale.

Similarly, Andrae *et al.* (2018) also set his absolute scale by taking $BC_{V,\odot} = -0.07$ mag and stating "bolometric correction needs a reference point to set the absolute scale". Setting up a private absolute scale for *BC* as done by Mamajek (2021) and Andrae *et al.* (2018) is not acceptable anymore since 2015. Despite IAU 2015 GAR B2, such private absolute scales do not mean recognizing the absolute *BC* scale set by IAU 2015 GAR B2, or IAU 2015 GAR B2 is not understood properly. Therefore, any *BC* value which is according to a private *BC* scale as implied by Cassagrande and VandenBerg (2018), Cox (2000), Andrae *et al.* (2018), Mamajek (2021) is not standard.

6.4. Color–Temperature and Temperature–Color Relations

It is a great advantage to have already calibrated $BC - T_{\rm eff}$ relations at various bands of a photometric system. This way, intrinsic color *vs.* temperature relations could automatically be set. Flower (1996) and Eker *et al.* (2020) had to compute first observed $(B-V)$ colors of the components from the light ratio (l_2/l_1) of components if they were available from light curve solutions in both *B*- and *V*-bands. Then, intrinsic $(B-V)_0$ colors are obtained using the reddening law $A_V/E(B-V) = R_V$ and definition of $E(B-V) = (B-V) - (B-V)_0$. Finally, after obtaining $(B-V)_0$ of components, $(B-V) - T_{\rm eff}$ relation is calibrated using published component effective temperatures.

In this study, the intrinsic colors of the component stars (data) are computed directly as the difference between the absolute magnitudes in Table 3. The computed intrinsic colors are then plotted in Fig. 9 where solid lines represent color–temperature relations as $(G_{\rm BP} - G_{\rm RP})_0 - T_{\rm eff}$, $(G - G_{\rm RP})_0 - T_{\rm eff}$, $(G - G_{\rm BP})_0 - T_{\rm eff}$, $(V-G)_0 - T_{\rm eff}$, and $(B-V)_0 - T_{\rm eff}$, respectively from top to bottom. At last, the

five color *vs.* effective temperature relations are directly computable as the difference of $BC-T_{\rm eff}$ relations. For example: $(B-V)_0-T_{\rm eff}$ relation is obtained as $BC_V(T_{\rm eff})-BC_B(T_{\rm eff})$ from the functions presented in Table 5. Similarly, for the other colors: $BC_G(T_{\rm eff})-BC_V(T_{\rm eff})$, $BC_{G_{\rm BP}}(T_{\rm eff})-BC_G(T_{\rm eff})$, $BC_{G_{\rm RP}}(T_{\rm eff})-BC_G(T_{\rm eff})$, $BC_{G_{\rm RP}}(T_{\rm eff})-BC_{G_{\rm BP}}(T_{\rm eff})$ give $(V-G)_0$ *vs.* $T_{\rm eff}$, $(G-G_{\rm BP})_0$ *vs.* $T_{\rm eff}$, $(G-G_{\rm RP})_0$ *vs.* $T_{\rm eff}$, $(G_{\rm BP}-G_{\rm RP})_0$ *vs.* $T_{\rm eff}$ relations, respectively.

As can be seen the solid lines (color–temperature relations) follow the trend of the data quite nicely. Especially, the upper two panels in Fig. 9, $(G_{\rm BP}-G_{\rm RP})_0$ and $(G-G_{\rm RP})_0$ are represented very nicely by the solid lines while the middle panel, $(G-G_{\rm BP})_0$, could only be considered successful for the medium hot and cooler stars ($\log T_{\rm eff} < 4.2$). Nevertheless, a small but a clear offset between the solid lines and data is obvious in the lowest two panels, $(V-G)_0$ and $(B-V)_0$, in Fig. 9. It has been already discussed in Section 4 that *B* and *V* data are less reliable compared the Gaia data. Moreover, if the number of data toward the cooler and hotter ends in Figs. 4 and 5 are compared, the Gaia bands appear relatively more crowded. Being less reliable and having lower number of data compared to Gaia bands toward both ends of the temperature scale, the $BC-T_{\rm eff}$ relations of the *B*- and *V*-bands appear to be the most probable cause of the offset seen in the lowest two panels of Fig. 9. This is because the solid lines are just the differences of the $BC-T_{\rm eff}$ relations and the bias caused by the less number of data appears not only effecting both ends but also changing the mean value of the *BC* values. Thus, the solid lines appear to be noticeably shifted causing the offset seen especially for *B*- and *V*-bands.

Therefore, only the solid lines in the upper two panels, $(G_{\rm BP}-G_{\rm RP})_0$ and $(G-G_{\rm RP})_0$, are found suitable to represent color–temperature relations which are to be included in Table 6 where they are presented together with the *BC* values produced from the polynomials in Table 5 as a function of spectral types and typical effective temperatures for main-sequence stars having metallicity $0.008 < Z < 0.040$. On the other hand, it is more practical for a user to have an effective temperature *vs.* color relation in order to estimate the effective temperature of a main-sequence star from an intrinsic color. For this, we have calibrated inverse relations only for $B-V$ for Johnson photometry and $G_{\rm BP}-G_{\rm RP}$ for Gaia photometry.

Effective temperatures of the DDEB sample of this study are plotted as a function of $(B-V)_0$ and $(G_{\rm BP}-G_{\rm RP})_0$ in Fig. 10. Data points are the same as the lowest and uppermost panels in Fig. 9, but the vertical and horizontal axis are interchanged and re-organized. The solid lines in Fig. 10 are the temperature–color relations which are re-predicted from intrinsic colors of DDEB marked in Fig. 10 unlike the color–temperature relations shown in Fig. 9 which are obtained from the differences of $BC-T_{\rm eff}$ relations. The temperature–color relations as polynomials are given in Table 8. Fourth-degree polynomials are found best to explain $(B-V)$ and $(G_{\rm BP}-G_{\rm RP})$ intrinsic colors of the main-sequence stars chosen from components of the DDEB sample of this study. Coefficients and errors associated

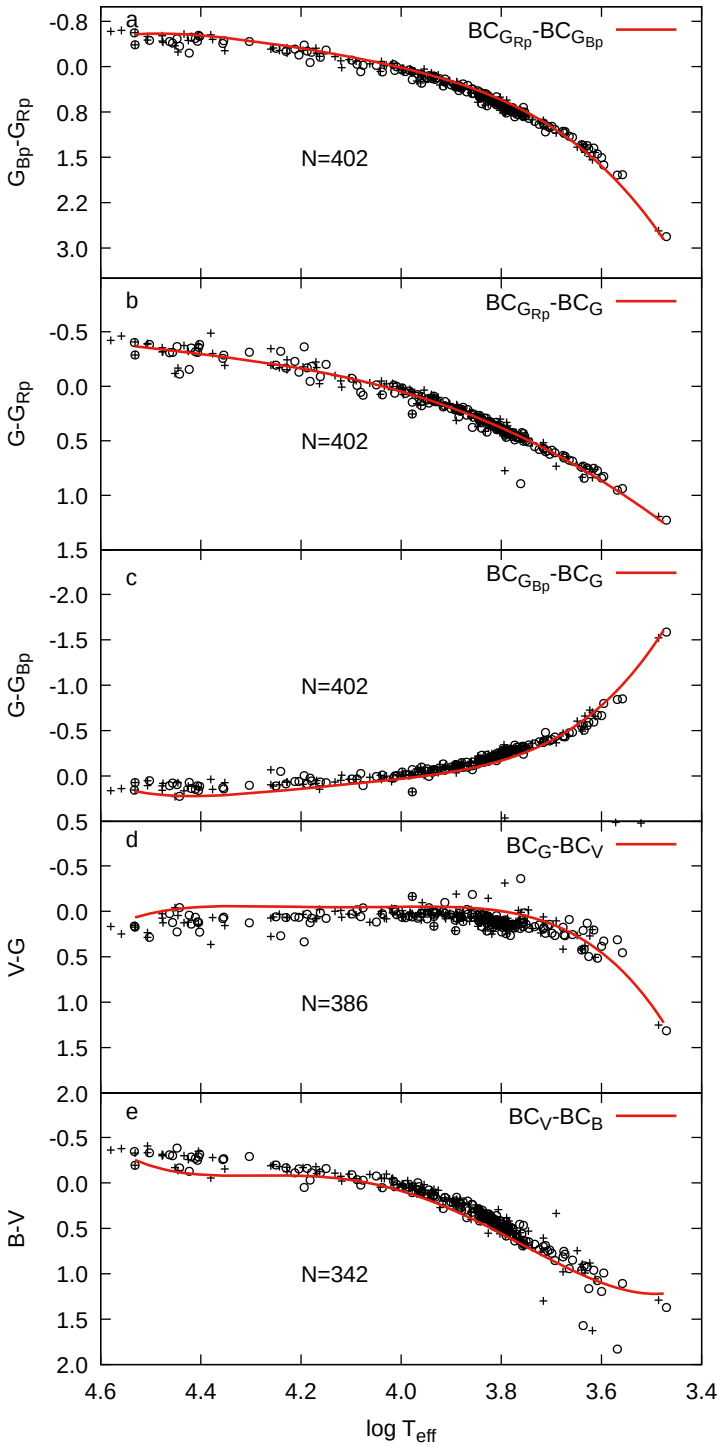

Fig. 9. Intrinsic colors of DDEB components as a function of log $T_{\rm eff}$, (+) for primary and (o) for secondary. Solid lines are main-sequence color *vs.* $T_{\rm eff}$ relations imposed by $BC-T_{\rm eff}$ relations.

are determined by the least-squares method and listed in Table 8 together with the ranges of their validity expressed in intrinsic colors as $-0.5 \leq (B-V)_0 \leq 1.5$ and $-0.6 \leq (G_{\rm BP}-G_{\rm RP})_0 \leq 1.7$.

T a b l e 8

Parameters of temperature *vs.* intrinsic color relations

$\log T_{\rm eff} = a + b\times(B-V)_0 + c\times(B-V)_0^2 + d\times(B-V)_0^3 + e\times(B-V)_0^4$				
a	b	c	d	e
4.05136	−0.902404	1.03912	−0.686631	0.144272
±0.005228	±0.01865	±0.06344	±0.1399	±0.07865
rms = 0.05091				
valid in the range $-0.5 \leq (B-V)_0 \leq 1.5$ mag				
$\log T_{\rm eff} = a + b\times(G_{\rm BP}-G_{\rm RP})_0 + c\times(G_{\rm BP}-G_{\rm RP})_0^2 + d\times(G_{\rm BP}-G_{\rm RP})_0^3 + e\times(G_{\rm BP}-G_{\rm RP})_0^4$				
a	b	c	d	e
4.04695	−0.595137	0.42341	−0.199622	0.0351755
±0.004102	±0.007874	±0.0211	±0.0211	±0.005871
rms = 0.0396				
valid in the range $-0.6 \leq (G_{\rm BP}-G_{\rm RP})_0 \leq 1.7$ mag				

Except for the four stars (components of V881 Per and 2MASS J19071662+463932), which are marked with their order number in Fig. 10a, the intrinsic $(B-V)$ colors are well represented by the predicted $T_{\rm eff}$ *vs.* color relation (solid line). The $T_{\rm eff}-$color relation by Eker *et al.* (2020), marked as dotted curve, and Mamajek (2021), marked as a dashed curves, are also plotted on the same figure just for comparison. It is clear in Fig. 10a that the solid line (this study) is more successful in representing data than the dotted and the dashed curves. Although both the dotted and the dashed curves are drawn to represent intrinsic $(B-V)$ colors up to 2.00, the reddest stars ($(B-V)_0 > 0.80$) are also not well represented by the dotted and dashed curves.

Unfortunately, there are no other full-range intrinsic $(G_{\rm BP}-G_{\rm RP})$ colors published for comparing temperature–color relation predicted in this study. The main-sequence $(G_{\rm BP}-G_{\rm RP})$ intrinsic colors of Mamajek (2021) cover a range of temperatures $2350 \leq T_{\rm eff} \leq 10\,700$ K, spectral types B9.5V to M9.5V and $(G_{\rm BP}-G_{\rm RP})$ from −1.2 to 4.86. The full range of $(G_{\rm BP}-G_{\rm RP})$ data is represented better by the $T_{\rm eff}-$color relation of this study. The dashed curve (Mamajek 2021) does not reach the hottest stars. Agreement between solid and dashed curves the middle temperatures are clear. The coolest stars are again better represented by $T_{\rm eff}-$color relation of this study than the dashed curve of (Mamajek 2021).

Intrinsic colors as a function of spectral types and effective temperatures computed according to the two $T_{\rm eff}-$color relations shown in Fig. 10 and listed in Ta-

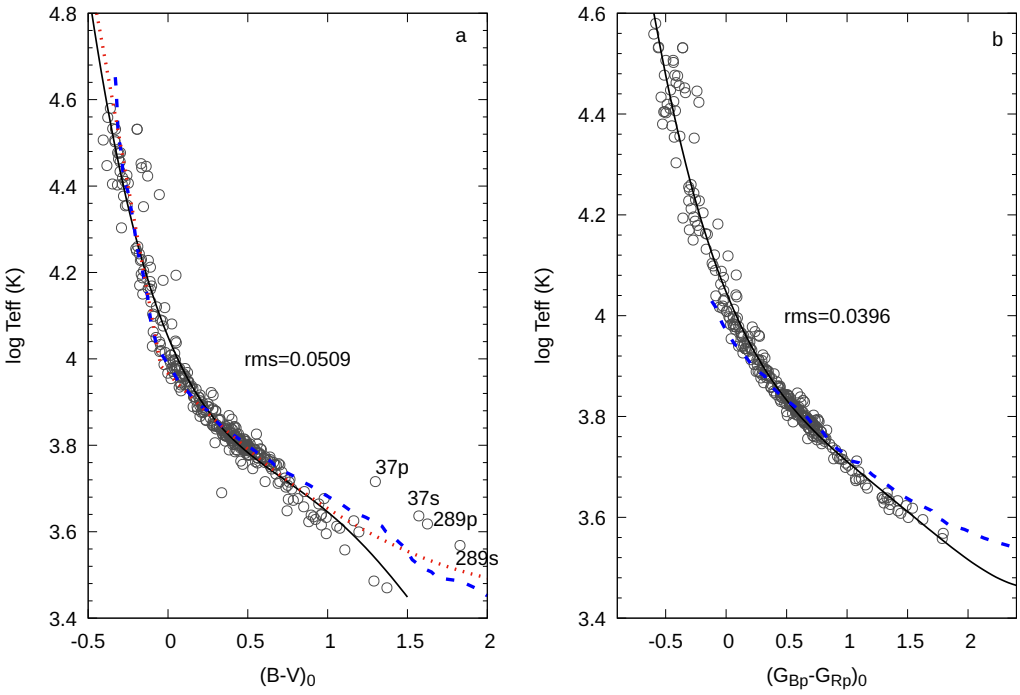

Fig. 10. $T_{\rm eff}-(B-V)_0$ (*a*) and $T_{\rm eff}-(G_{\rm BP}-G_{\rm RP})_0$ (*b*) relations. The best-fitting models (Table 8) are shown by solid lines where the dotted curve (only *left panel*) is from Eker *et al.* (2020) and dashed curves in *both panels* are from Mamajek (2021).

ble 8 are also included in Table 6 . Now, it is important to notice that Table 6 has four columns with three intrinsic colors, first two, $(G-G_{\rm RP})_0$ and $(G_{\rm BP}-G_{\rm RP})_0$, of them (columns 8 and 9) are produced by subtracting the proper *BC* columns in the same table as described before, that is directly from the $BC-T_{\rm eff}$ relations listed in Table 5 and the last two ($(G_{\rm BP}-G_{\rm RP})_0$ and $(B-V)_0$) of them (columns 10 and 11) are produced from the $T_{\rm eff}-$color relations listed in Table 8, which are produced directly from the intrinsic colors of DDEB stars.

Having the same intrinsic color, $(G_{\rm BP}-G_{\rm RP})_0$, produced by the two different methods described above is good for fine testing of the new method on producing intrinsic colors since in the first approximation the three intrinsic colors, $(B-V)_0$, $(V-G)_0$, and $(G-G_{\rm BP})_0$, produced by the new method were already eliminated by eye inspections in Fig. 9. Eliminations of these intrinsic colors indicate that $BC-T_{\rm eff}$ relation in Table 5 are not sufficiently accurate enough to produce intrinsic colors while they are shown reliable for estimating (if one of them is used) a standard L and improving its accuracy (if multiples of them are used) as demonstrated in Fig. 8.

The mean difference between the two columns in Table 6 giving the same intrinsic color, $(G_{\rm BP}-G_{\rm RP})_0$, produced by the different methods (columns 9 and 10) could be used as a parameter to indicate reliability of the new method with respect

to the classical method. The existing numbers in Table 6 indicate a 0.06 mag difference for this study. Minimizing this value in a future study would definitely indicate a noticeable improvement of the new method for producing reliable intrinsic colors from $BC-T_{\rm eff}$ relations. Not only the intrinsic colors, but also the predicted standard L would be improved because $BC-T_{\rm eff}$ relations themselves would also be improved automatically. An ideal case is that both methods are producing the same numbers, that is the mean difference between the two columns producing the same color should be zero or negligible. For that we encourage future researchers not only to increase the number of filters, photometric systems and the number of DDEB stars to be used (especially toward both ends of the temperature scale) in their study but also to find a method for homogenizing the systemic brightness' or set up an observing program to obtain consistent total brightness of systems for inconsistent bands to improve their consistency – like Gaia bands.

6.5. Reddening Law and Color–Color Relations

It is possible to check the best value of the passband-based parameter $R(\xi)$ by modeling the $A(\xi)-E(B-V)$ relation, which is given as:

$$R_\xi = \frac{A(\xi)}{E(B-V)}, \tag{13}$$

$$E(B-V) = A(B) - A(V). \tag{14}$$

Using passband based $A(\xi)$ values from Table 3 and using Eq.(14), color excess *vs.* interstellar dimming relations for Johnson and Gaia passbands have been constructed and shown in Figs. 11 and 12 together with standard deviation (*rms*) from the correlation equations on each plot. The correlation is actually in the form $f(x) = a + bx$, where a is the constant term and b is $R(\xi)$. In all correlations, the constant term is zero under Eq.(13). The most commonly used parameter, $R(V)$ is found to be 3.012 ± 0.002, which is slightly smaller than the common average value for the solar neighborhood in the Milky Way ($R(V) = 3.1$). For the Johnson-B filter, this relation is predicted as $R(B) = 4.012 \pm 0.002$ and for the Gaia passbands, they are found as $R(G) = 2.872 \pm 0.013$, $R(G_{\rm BP}) = 3.494 \pm 0.009$ and $R(G_{\rm RP}) = 1.885 \pm 0.001$. It is worth noting that the errors of the parameters ($R(\xi)$) are found to be relatively small (< 0.1 per cent for $A(V)$ and $A(B)-E(B-V)$ relations, < 0.7 per cent for $A(G)$, $A(G_{\rm BP})$ and $A(G_{\rm RP})-E(B-V)$ relations). The accuracy of the correlation parameter is relatively better for the interstellar dimming in Gaia passbands versus Gaia color excess except for $A(G_{\rm RP})-E(G_{\rm BP}-G_{\rm RP})$ which is ≈ 0.8 per cent.

Other useful relations used in photometry are the color–color diagrams and color excess relations between colors based on certain photometric systems. Color excess relations between different colors may show the direction of interstellar extinction on the diagram. Having this information on the color–color diagrams per-

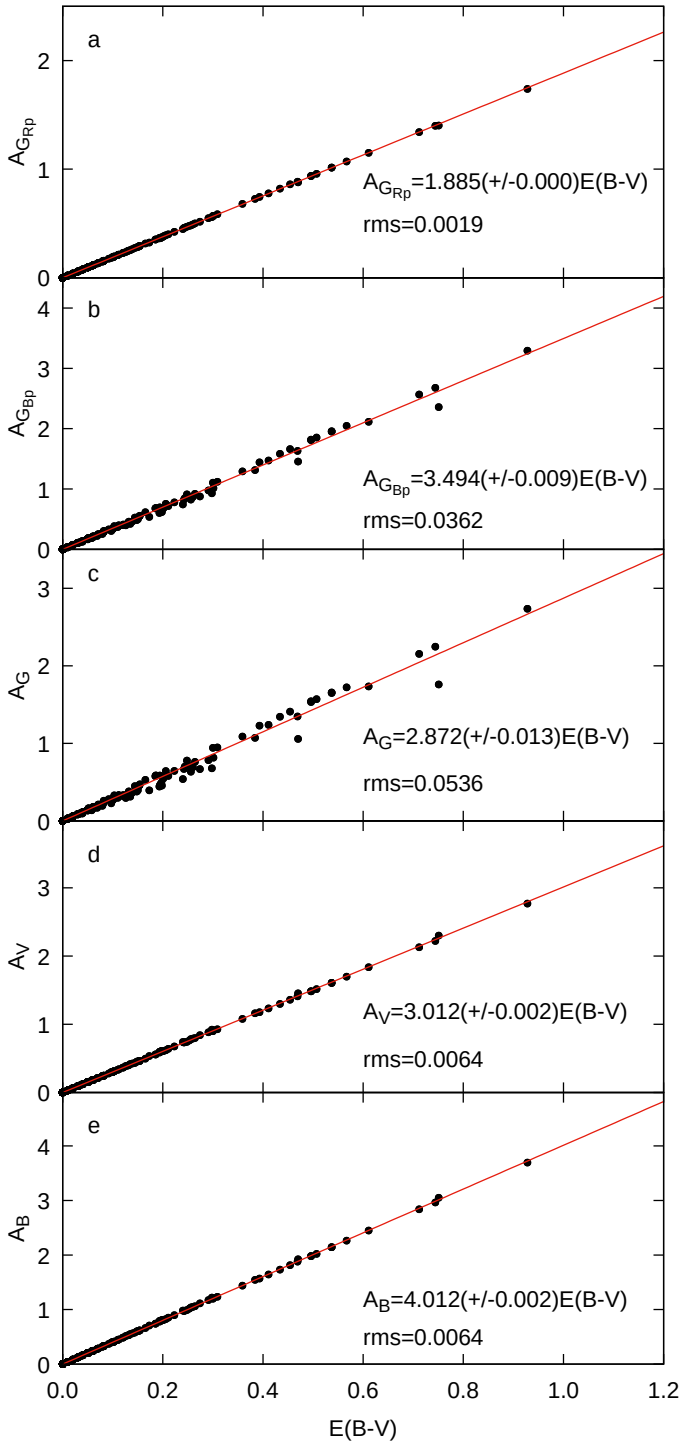

Fig. 11. Correlation of interstellar dimming (A_ξ) with $E(B-V)$ color excess in Johnson and Gaia passbands.

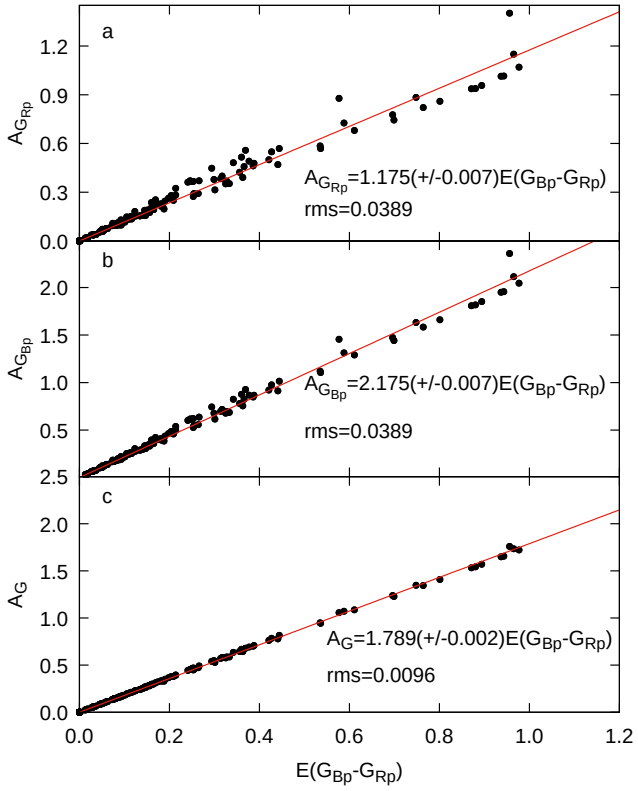

Fig. 12. Correlation of interstellar dimming (A_ξ) with $E(G_{\rm BP}-G_{\rm RP})$ color excess in Gaia passbands.

mits users to define unreddened colors of stars by tracing back the extinction direction up to the intersecting point on the line of unreddened main-sequence stars.

Fig. 13 shows color–color and color excess *vs.* color excess diagrams for the nearby main-sequence stars as predicted from the DDEB sample of this study for various Gaia passbands. Fig. 13a compares $(G-G_{\rm BP})-(G_{\rm BP}-G_{\rm RP})$ relation of this study to the one given by Arenou *et al.* (2018). A very good agreement between them is very clear. Nevertheless, the color–color curves for Gaia passbands of main-sequence stars are almost parallel to the direction of interstellar reddening which creates difficulties in the determination of unreddened colors by going back along the reddening direction. Among the color–color relations in Fig. 13, $(G-G_{\rm RP})-(G_{\rm BP}-G)$ (panel c) seem to be more suitable for searching intrinsic colors toward cooler stars since the reddest part is un-parallel to the reddening direction.

The ratio of color excess of $E(G-G_{\rm BP})/E(G_{\rm BP}-G_{\rm RP})$, $E(G-G_{\rm RP})/E(G_{\rm BP}-G_{\rm RP})$ and $E(G-G_{\rm BP})/E(G_{\rm BP}-G_{\rm RP})$ in panels d, e and f of Fig. 13 gives the direction of extinction in the color–color diagrams shown in panels a, b and c, respectively. The solid lines shown with red color are the best fits to all data while

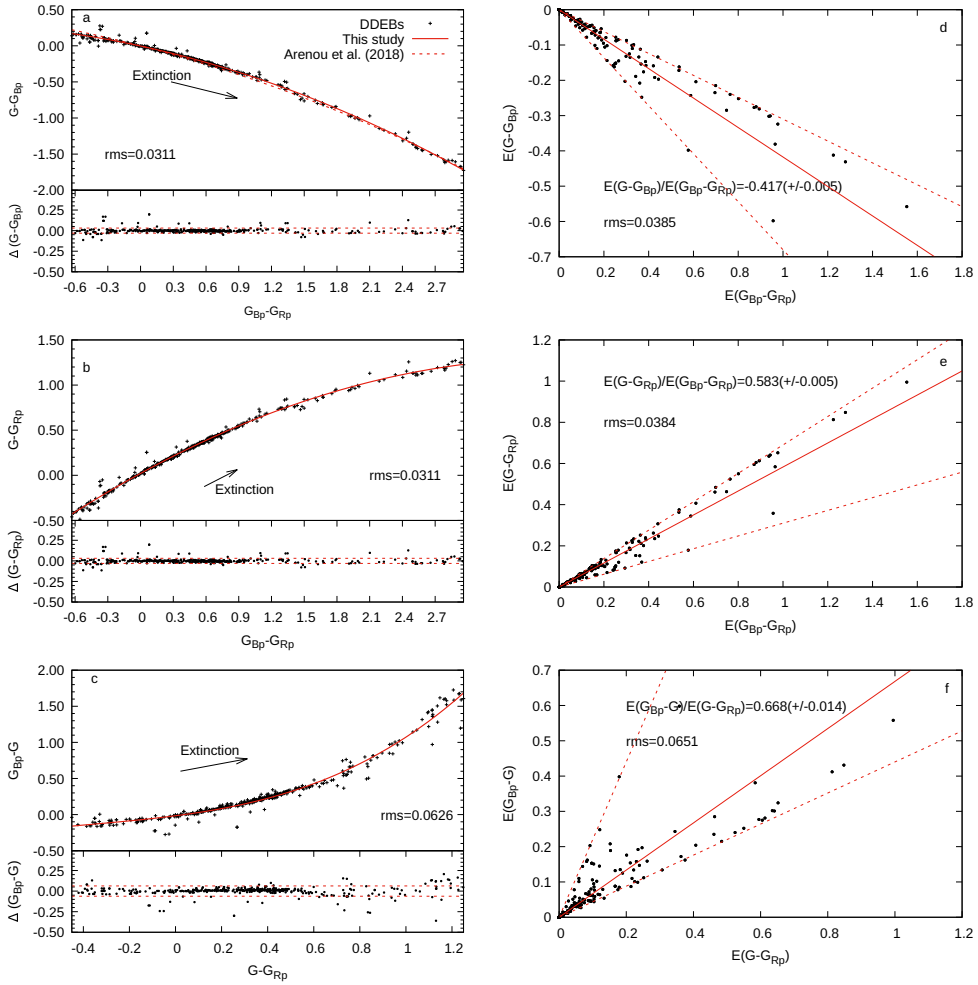

Fig. 13. Color–color (*left panels*) and color excess *vs.* color excess relations (*right panels*) in Gaia-bands for nearby main-sequence stars. Equations and *rms* values in the right panel refer to the solid lines. Dashed lines below each panel in the left are 1σ deviations while the dashed lines on the right indicate the borders of the most extreme values.

the dashed lines represent the borders of the data. These borders refer to the limits. Since a unique reddening direction in a color–color diagram for all stars in our sample is not expected, it is normal to see a certain interval of the reddening direction values in different Gaia EDR3 passbands. The slope of the solid lines refers to the average value for the relevant color excess ratio defining the direction of reddening in color–color diagrams. The slope of the dashed lines changes between -0.31 and -0.68, 0.44 and 2.2, and 0.31 and 0.69 for $E(G-G_{\rm BP})/E(G_{\rm BP}-G_{\rm RP})$ (panel d), $E(G-G_{\rm RP})/E(G_{\rm BP}-G_{\rm RP})$ (panel e) and $E(G-G_{\rm BP})/E(G_{\rm BP}-G_{\rm RP})$ (panel f) ratios, respectively. Therefore, the reddening direction shown by an arrow in the left panels is not unique. Direction of the arrow may change for different galactic directions.

7. Conclusions

- A simplified SED model is established for predicting component light contributions of binaries and their interstellar extinctions.
- The component light contributions predicted by the simplified SED model in *B*- and *V*-bands of Johnson photometry are tested by comparing to the *B*- and *V*-band light contributions predicted from the light curve solutions of DDEB. The simplified SED model is found very successful and reliable in predicting component light contributions according to test in this study.
- 209 DDEB are found eligible to provide a binary SED model without complexities (third light or any excess flux) which may spoil the SED of the binary. Then, using component contributions, which are produced from the simplified SED model, empirical standard *BC*s are produced by a method described by Eker *et al.* (2020).
- The empirical standard *BC* values are used in calibrating empirical standard $BC-T_{\rm eff}$ relations in *B*, *V*, *G*, $G_{\rm BP}$- and $G_{\rm RP}$-bands. The most accurate $BC-T_{\rm eff}$ relation ever discussed is produced and presented.
- Empirical standard $BC-T_{\rm eff}$ relations of five passbands are used for predicting standard stellar L. They are compared to the L calculated from the observed R and $T_{\rm eff}$. If a standard L is predicted from a single $BC-T_{\rm eff}$ relation of a given band, propagated errors indicate that it cannot be more accurate than about 10 cent. Accuracy of the predicted L increases by increasing the number of $BC-T_{\rm eff}$ relations at various passbands. A standard L with an uncertainty as low as one per cent (peak at ≈ 2.5 per cent), is possible.
- Multiband $BC-T_{\rm eff}$ relations are shown to be practical to obtain intrinsic color–temperature relations. Intrinsic color *vs.* temperature relations could be produced directly from differences of $BC-T_{\rm eff}$ relations.
- Inverse color–temperature relations involving $(B-V)_0$ and $(G_{\rm BP}-G_{\rm RP})_0$ are produced, useful if one wants to calculate effective temperature of a main-sequence star from its $(B-V)_0$ and $(G_{\rm BP}-G_{\rm RP})_0$.
- Reddening laws, color–color and color excess *vs.* color excess relations involving Johnson *B*, *V* and Gaia passbands covering all spectral classes of the main-sequence from the DDEB sample of this study are presented.

Acknowledgements. This work uses the VizieR catalog access tool, CDS, Strasbourg, France, the SIMBAD database, operated at CDS, Strasbourg, France. This work presents results from the European Space Agency (ESA) space mission,

Gaia. Gaia data are being processed by the Gaia Data Processing and Analysis Consortium (DPAC). Funding for the DPAC is provided by national institutions, in particular the institutions participating in the Gaia MultiLateral Agreement (MLA). The Gaia mission website is *https://www.cosmos.esa.int/gaia*. The Gaia archive website is https://archives.esac.esa.int/gaia. We thank to Associate Prof. Mustafa Caner for proof reading and correcting English grammar and linguistics. We are also grateful to the anonymous referee who carefully read our paper and made very meaningful comments that made us improve its clearance.

REFERENCES

Andrae, R., Fouesneau, M., Creevey, O., *et al.* 2018, *A&A*, **616**, A8.
Arenou, F., Luri, X., Babusiaux, C., *et al.* 2018, *A&A*, **616**, A17.
Bessell, M.S. 1990, *PASP*, **102**, 1181.
Bessell, M.S., Castelli, F., and Plez, B. 1998, *A&A*, **333**, 231.
Bressan, A., Marigo, P., Girardi, L., *et al.* 2012, *MNRAS*, **427**, 127.
Casagrande, L., and VandenBerg, D.A. 2018, *MNRAS*, **475**, 5023.
Cayrel, R., Castelli, F., Katz, *et al.* 1997, *Proceedings of the ESA Symposium*, **402**, 433.
Chen, Y., Girardi, L., Fu, X., *et al.* 2019, *A&A*, **632**, A105.
Clayton, D.D. 1968, "Principles of stellar evolution and nucleosynthesis".
Code, A.D., Davis, J., Bless, R.C., and Brown, R.H. 1976, *ApJ*, **203**, 417.
Cox, A.N. 2000, "Allen's astrophysical quantities".
Eker, Z., Soydugan, F., Bilir, S., *et al.* 2020, *MNRAS*, **496**, 3887.
Eker, Z., Bakış, V., Bilir, S., *et al.* 2018, *MNRAS*, **479**, 5491.
Eker, Z., Bakış, V., Soydugan, F., and Bilir, S. 2021a, *MNRAS*, **503**, 4231.
Eker, Z., Soydugan, F., Bilir, S., and Bakış, V. 2021b, *MNRAS*, **507**, 3583.
Evans, D.W.,Riello, M., De Angeli, F., *et al.* 2018, *A&A*, **616**, A4.
Fitzpatrick, E.L. 1999, *PASP*, **111**, 63.
Flower, P.J. 1977, *A&A*, **54**, 31.
Flower, P.J. 1996, *ApJ*, **469**, 355.
Gaia Collaboration, Brown, A.G.A., Vallenari, A. *et al.* 2018, *A&A*, **616**, A1.
Girardi, L., Bertelli, G., Bressan, A., *et al.* 2002, *MNRAS*, **391**, 195.
Girardi, L., Dalcanton, J., Williams, B., *et al.* 2008, *PASP*, **120**, 583.
Graczyk, D., Pietrzyński, G., Gieren, W., *et al.* 2019, *ApJ*, **872**, 85.
Heintze, J.R.W. 1973, *Proceedings of IAU Symposium*, **54**, 231.
Johnson, H.L. 1964, *Boletin de los Observatorios Tonantzintla y Tacubaya*, **3**, 305.
Johnson, H.L. 1966, *Ann. Rev. Astron. Astrophys*, **4**, 193.
Jordi, C., Gebran, M., Carrasco, J.M., *et al.* 2010, *A&A*, **532**, 48.
Kuiper, G.P. 1938, *ApJ*, **88**, 429.
Lacy, C.H.S., Torres, G., Wolf, M., and Burks, C.L. 2014, *AJ*, **147**, 1.
Martins, F., and Plez, B. 2006, *A&A*, **457**, 637.
McDonald, J.K, and Underhill, A.B. 1952, *ApJ*, **115**, 577.
Pecaut, M.J., and Mamajek, E.E. 2013, *ApJS*, **208**, 9.
Pedersen, M.G., Escorza, A., Pápics, P.I., and Aerts, C. 2020, *MNRAS*, **495**, 2738.
Popper, D.M. 1959, *ApJ*, **129**, 647.
Smak, J. 1966, *Acta Astron.*, **16**, 1.
Sung, H., Lim, B., Bessell, M.S., *et al.* 2013, *Journal of Korean Astronomical Society*, **46**, 103.
Tomasella, L., Munari, U., Siviero, *et al.* 2008, *A&A*, **480**, 465.
Torres, G. 2010, *AJ*, **140**, 1158.
Weidemann, V., and Bues, I. 1967, *Zeitschrift für Astrophysik*, **67**, 415.

Wenger, M., *et al.* 2000, *A&AS*, **143**, 9.
Wildey, R.L. 1963, *Nature*, **199**, 988.
Wilmor, Ch.N.A. 2018, *ApJS*, **236**, 47.